

13

Electromechanics of Soft Resistive and Capacitive Tactile Sensors

Zhengjie Li¹, Sangjun Kim², Zheliang Wang¹, Zhengtao Zhu³, and Nanshu Lu^{1,2,4,5,6}

¹The University of Texas at Austin, Department of Aerospace Engineering and Engineering Mechanics, Austin, TX 78712, USA

²The University of Texas at Austin, Department of Mechanical Engineering, Austin, TX 78712, USA

³South Dakota School of Mines & Technology, Department of Chemistry, Biology, and Health Sciences, Rapid City, SD 57701, USA

⁴The University of Texas at Austin, Department of Electrical and Computer Engineering, Austin, TX 78712, USA

⁵The University of Texas at Austin, Department of Biomedical Engineering, Austin, TX 78712, USA

⁶The University of Texas at Austin, Texas Materials Institute, Austin, TX 78712, USA

13.1 Introduction

13.1.1 Overview of Tactile Sensors

In the fascinating realm of human physiology, the skin stands out as the largest and one of the most versatile organs [1], endowed with remarkable properties that have inspired technological innovation, particularly in the development of electronic skins (e-skins). This extraordinary organ boasts a tactile-sensing capability with a force detection threshold as delicate as 1 mN [2], coupled with a high sensitivity of nearly 2 kPa^{-1} , extending up to forces of 10 N [3] or pressures of 70 kPa [4]. Beyond its touch sensitivity, the human skin exhibits an impressive stretchability, capable of fully recovering after elongating up to 40% of its original length [5, 6]. This elasticity is complemented by the skin's ability to discern pressure even amidst the complex interplay of simultaneous tension, shear, and twist forces. These intricate sensory and mechanical characteristics of human skin not only highlight its biological sophistication but also serve as a blueprint for the design and engineering of advanced tactile-sensing e-skins, aiming to replicate the skin's multifaceted functionalities in artificial systems.

E-skins have a broad array of applications centered around both humans and robotics [2, 7–10]. Selected examples are displayed in Figure 13.1 [11–19]. For humans, the applications span pulse sensing [12, 20, 21], prosthetics [13, 22], human–machine interaction (HMI) [14, 23], and biometric authentication such as fingerprint and typing style recognition [15, 24]. For robotic applications, e-skins can aid in identifying the shape or stiffness of objects [16, 17, 25], facilitating precise

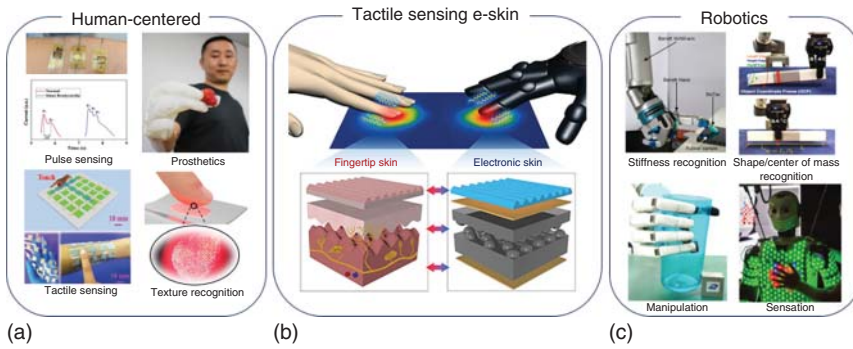

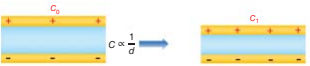






Figure 13.1 Tactile-sensing e-skin and its applications. (b): Tactile-sensing human skin versus e-skin. Source: Reproduced with permission from Ref. [11]. Copyright 2015 AAAS. (a): human-centered applications including pulse sensing. Source: Reproduced with permission from Ref. [12]. Copyright 2022 John Wiley & Sons, prosthesis. Reproduced with permission from Ref. [13]. Copyright 2022, Springer; tactile sensing. Reproduced with permission from Ref. [14], Copyright 2020 Elsevier; and texture recognition. Reproduced with permission from Ref. [15]/Springer Nature/CC BY 4.0. (c): robotics applications including stiffness recognition. Source: Reproduced with permission from Ref. [16]/Frontiers Media S.A./CC BY 3.0. Reproduced with permission from Ref. [17]. Copyright 2019 Springer; manipulation. Reproduced with permission from Ref. [18]. Copyright 2022 Wiley; sensation. Reproduced with permission from Ref. [19]. Copyright 2020 MDPI.

manipulation [18, 26], and endowing robots with somatosensory capabilities [19, 27].

As a central component of e-skins, mechanically soft tactile sensors have been the subject of extensive research for decades [28–32]. Recent advances in tactile sensors commonly adopt pressure-sensing mechanisms, including resistive [33–37], capacitive [38–44], iontronic [45], piezoelectric [46–48], triboelectric [49], optical [50, 51], and magnetoelastic [52] readouts, as summarized in Table 13.1. Under compression, different pressure-sensing materials generate a change in electrical resistance ΔR , capacitance ΔC , capacitance of electrical double layer ΔC , charge Δq , transmittance of light ΔI , or magnetic flux density ΔB , respectively. Each mechanism possesses its own set of advantages and disadvantages, as outlined in Table 13.1. This chapter only focuses on resistive tactile sensors (RTSs) and capacitive tactile sensors (CTSs) because they rely on basic materials and readout circuits for pressure sensing with a long history. In addition, they can maintain a stable performance over extended time [28, 53]. Compared with resistive and capacitive tactile sensors, iontronic tactile sensors only emerged a decade ago. They leverage the supercapacitive nature of electrical double layers achieved through the movement of ions within an ionically conductive material. Iontronic sensors can be ultrathin, optically transparent, mechanically soft, and highly sensitive over a large pressure range. But they are sensitive to environmental factors such as temperature, humidity, and exposure to chemicals and may suffer from ion migration over time [54]. Moreover, many electrolytic liquids used in iontronic sensors are not biocompatible [55]. Piezoelectric and triboelectric sensors do not require input power, but they are only suitable for

Table 13.1 Summary of tactile sensors: mechanism, advantages, and disadvantages.

Sensor type	Advantages	Limitations
Piezoresistive (ΔR) 	<ul style="list-style-type: none"> • Simple structure, facile fabrication • High pressure sensitivity • Easy signal readout and collection 	<ul style="list-style-type: none"> • Large hysteresis • Sensitive to temperature • DC power consumption
Capacitive (ΔC) 	<ul style="list-style-type: none"> • Simple structure, facile fabrication • High pressure sensitivity • Temperature insensitivity • Low power consumption 	<ul style="list-style-type: none"> • Decayed sensitivity with increasing pressure • Sensitive to parasitic capacitance • Sensitive to body loading
Iontronic (ΔC) 	<ul style="list-style-type: none"> • High sensitivity over larger pressure range • Optical transparency 	<ul style="list-style-type: none"> • Concerns in electrochemical stability • Sensitive to temperature and humidity • Frequency relaxation due to slow motion of ions under AC field
Piezoelectric/ Triboelectric (Δq) 	<ul style="list-style-type: none"> • Self-powered • Ideal for vibration sensing • Fast response 	<ul style="list-style-type: none"> • Not suitable for static pressure detection • Complex readout circuits • Triboelectric devices are sensitive to humidity
Optical (ΔI) 	<ul style="list-style-type: none"> • Simple wiring • Low drift 	<ul style="list-style-type: none"> • High power consumption • Contamination from ambient light • Signal attenuation due to misalignment
Magnetoelastic (ΔB) 	<ul style="list-style-type: none"> • No encapsulation required for chemical environment • Durability 	<ul style="list-style-type: none"> • Complex magnetization effect in the sensor • Less sensitive to pressure due to weak magnetoelastic effects

measuring dynamic pressures such as pulses or vibrations, and triboelectric sensors are sensitive to humidity and temperature [56]. Optical sensors are simple to wire up and almost immune from signal drift, but they require a high power input, and optical signals may be polluted by ambient light [57]. Magnetoelastic sensors can be used in chemical environments with high durability, but they have limited sensitivity due to weak magnetoelastic effects [52].

Traditional resistive and capacitive tactile sensors suffer from a lack of flexibility and stretchability—unlike natural human skin. This results in some limitations when used on surfaces that are curved or highly deformable. The lack of stretchability means these traditional sensors can either separate from the surface they are attached to or even break when they are stretched excessively [58, 59]. To overcome these limitations, it is critical to incorporate thinness and stretchability into the sensor design to transform conventional tactile sensors into e-skins. Such a design ensures the sensors maintain conformal, or matching, contact with the surface. This not only boosts the sensor's accuracy and reliability in data collection and feedback but also imparts unique adaptability. This adaptability enables the stretchable surface to adjust to various shapes and movements, enhancing its responsiveness to different tasks [60–62]. Therefore, stretchable e-skins surpass the challenges posed by traditional sensors. It aligns e-skin technology closer to the mechanical properties of human skin while enabling its use on surfaces with various shapes and contours to perform a wide range of functions.

13.1.2 Bottlenecks of Soft Resistive and Capacitive Tactile Sensors

Years of research have significantly improved the fundamental capabilities of resistive and capacitive pressure sensors. This includes enhancements in sensitivity, sensing range, linearity, and response time through the materials and structural innovations, which have already been well summarized in a few recent review articles [57, 63–66]. Despite these advancements, Figure 13.2 illustrates two outstanding obstacles with soft resistive and capacitive pressure sensors: a decrease in sensitivity as pressure increases [67–69], and interference caused by lateral deformation [43, 64, 70]. Figure 13.2a exhibits the simplest resistive and capacitive sensors set up with parallel electrodes. The area of these electrodes is represented by “ A ”, and “ d ” represents the distance between them. These sensors are subjected to a normal pressure labeled as “ P ”. The lateral tensile strain is labeled as “ ϵ ” in Figure 13.2b.

For a RTS, the resistance of the piezoresistive material sandwiched between the electrodes can be expressed as

$$R = \rho \frac{d_R}{A_R} \quad (13.1)$$

where R is the resistance of the piezoresistive material and ρ is its resistivity. Since resistance is measured under a constant DC voltage “ U ” and given the well-known Ohm's Law:

$$I = \frac{U}{R} = \frac{UA_R}{\rho d_R} \quad (13.2)$$

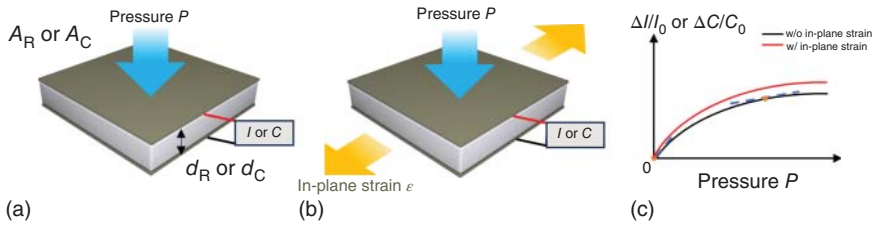


Figure 13.2 Two long-lasting bottlenecks in the stretchable resistive and capacitive tactile sensors. (a) Schematics of the resistive or capacitive tactile sensor subjected to pressure. (b) Schematics of the resistive (capacitive) tactile sensor upon pressure and in-plane stretch. (c) Relative change of current or capacitance as a function of pressure without and with in-plane stretch.

where I is the measured current response, the output of piezoresistive sensors is often plotted as I versus pressure instead of R versus pressure, as shown in Figure 13.2c.

The sensitivity of RTS is therefore the slope of the curve, which is given by:

$$S = \frac{d\left(\frac{\Delta I}{I_0}\right)}{dP} \quad (13.3)$$

where I_0 represents the initial current measured before pressure P is applied.

For a CTS with parallel electrodes sandwiching a dielectric material, the capacitance can be expressed as:

$$C = k\epsilon_0 \frac{A_C}{d_C} \quad (13.4)$$

where k is the dielectric constant and ϵ_0 is the permittivity of vacuum. The sensitivity of CTS is therefore the slope of the curve, which is given by:

$$S = \frac{d\left(\frac{\Delta C}{C_0}\right)}{dP} \quad (13.5)$$

where C_0 is the initial capacitance of the CTS before P is applied.

Both RTS and CTS exhibit nonlinear pressure responses, as illustrated in Figure 13.2c. While the curve may start with a large slope at small pressure, it can quickly bend with diminishing sensitivity. This phenomenon is called the pressure-sensitivity trade-off, which is attributable to a marked increase in the effective stiffness of the pressure-sensing material under large pressure, accompanied by boundary confinement from electrodes [64, 68].

The second bottleneck is called stretch interference, meaning that when pressure and lateral stretch are simultaneously applied to the sensor, as illustrated in Figure 13.2b, the lateral stretch may skew the pressure response, as indicated by the red curve in Figure 13.2c. As a result, the lateral stretch would cause inaccurate pressure readings. Both RTS and CTS suffer from this bottleneck because both the R given in Eq. (13.1) and the C given in Eq. (13.4) depend on the sensor's geometric dimensions, A and d , both of which are affected by the lateral stretch (d is affected due to the Poisson's effect).

To mitigate issues related to pressure-sensitivity trade-off and stretch interference, diverse structural [42, 44, 71, 72] and material strategies [71, 73, 74] have been researched for soft RTS and CTS. Notable structural designs are micro-patterned surfaces [44], nanowire networks [71], foams [72], and textiles [42]. Common materials used include conductive composites [73], polymers [74], and nanomaterials [71]. Comprehensive documentation of the materials, structures, sensor performance, and applications of these sensors exists in several review papers [75, 76]. Therefore, this book chapter does not focus on those aspects. Despite a wealth of publications, there still lacks a systematic electromechanics understanding of why these strategies are effective and where the future research on RTS and CTS should head. So, the objective of this chapter is to outline the existing electromechanical models in soft resistive and capacitive tactile sensors, including simplified circuit models, resistivity and dielectric constant of soft composites, and how these properties change under applied pressure. Additionally, the chapter will discuss the impacts of different structural designs. The hope is that this basic discussion could facilitate cross-disciplinary description and understanding of soft RTS and CTS among materials scientists, mechanical engineers, and electrical professionals. Also, this chapter seeks to guide researchers in assessing and predicting sensor performance and identify directions for future sensor research and development to ultimately overcome the challenges of building human-like e-skins.

13.2 Resistive Tactile Sensors

13.2.1 Introduction of Resistive Tactile Sensors

Flexible RTS can be categorized into three types based on the materials/structures of the sensor – microstructured contact, bulk conductive nanocomposites, and porous conductive materials, as shown in Figures 13.3a–c. The microstructured contact-based RTS is highly sensitive at low pressure but has a limited pressure-sensing range [77], while the RTS based on the bulk conductive nanocomposites exhibits relatively low sensitivity but can operate over a wide pressure range [78]. The device based on the porous conductive materials can have varied piezoresistive response performance [79]. Popular materials for these sensors are composites of elastomers and conductive fillers [80], although fabrics [81] and network of nanowires [82] or 2D materials [83] have also been explored. The complexity of the material parameters increases from microstructured contact to bulk conductive nanocomposites and porous conductive material.

The resistance of the RTS can be modeled by the equivalent circuit of contact resistance and bulk resistance connected in series (Figure 13.3d), i.e.

$$R = 2R_c + R_b \quad (13.6)$$

where R is the total resistance of the sensor, R_c is the contact resistance, and R_b is the bulk resistance of the sensing layer. The piezoresistive response of the sensor can be analyzed and modeled by changes in contact resistance R_c and sensing layer resistance R_b under compressive pressure.



Figure 13.3 Schematics of three representative types of RTS. (a) Microstructured contact. (b) Bulk conductive nanocomposites. (c) Porous conductive materials. (d) A simple equivalent circuit of RTS.

13.2.2 Resistive Tactile Sensors Based on Microstructured Contact

For RTS based on the microstructured contact, the bulk resistance (R_b) of the conductive elastomer can be negligible, and the total resistance (R) of the device equals the contact resistance (R_c). In this scenario, the filler concentration of the conductive elastomer needs to be sufficiently high to achieve negligibly low bulk resistance, so that the device performance is not affected by the filler concentration. The piezoresistive response with applied pressure largely depends on the area of the contact and Young's modulus of the conductive elastomer.

The relative resistance changes of the RTS based on the microstructured contact can be expressed as follows:

$$\frac{\Delta R}{R} = \frac{(2R_{c0} + R_{b0}) - (2R_c + R_b)}{2R_{c0} + R_{b0}} = \frac{R_{c0} - R_c}{R_{c0}} = 1 - \frac{R_c}{R_{c0}} \quad (13.7)$$

where $\Delta R = R_0 - R$, R_0 , R_{c0} , and R_{b0} are the initial total resistance, initial contact resistance, and initial bulk resistance, respectively, R , R_c , and R_b are the total resistance, contact resistance, and bulk resistance under pressure, respectively.

The piezoresistive response can be modeled using contact theory [84–89]. Figure 13.4a shows two conductive elastic spheres composed of conductive filler (e.g. silver particles) and elastomer (e.g. polydimethylsiloxane [PDMS]) in contact with each other under a normal force (N). Both spheres undergo a local contact deformation, creating a flat circular contact surface of radius a . Considering the high filler concentration in the composite, the resistivity of the spheres, ρ_b , is significantly small, and the resistance of the system is governed by the contact resistance. At the interfacial contact area, as shown in Figure 13.4b, the contact resistance arises from two possible mechanisms – constriction resistance R_{cr} and tunneling resistance R_t .

$$R_c = R_{cr} + R_t \quad (13.8)$$

where R_c is the contact resistance, R_{cr} is the constriction resistance, and R_t is the tunneling resistance.

Constriction resistance originates from the roughness of the interfacial contact area at the micro- or nanoscale, which results in an effective interfacial contact area less than the cross-section of the interface [90]. The constriction resistance for a circular contact can be derived as [88],

$$R_{cr} = \frac{\rho_b}{2a} = \frac{\rho_b}{2\sqrt{\frac{A}{\pi}}} = \frac{\rho_b}{2} \left(\frac{\pi}{A} \right)^{1/2} \quad (13.9)$$

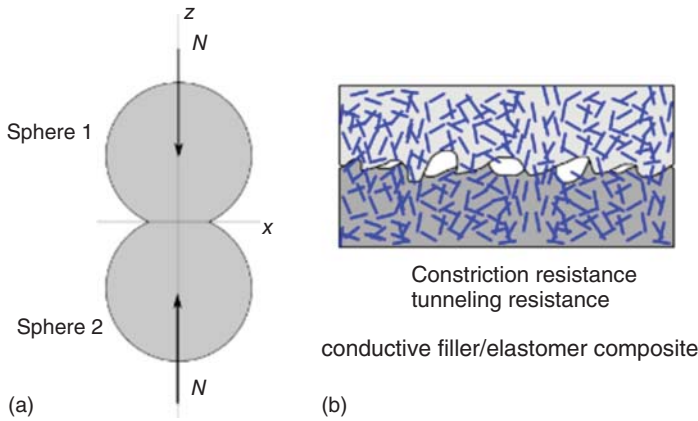


Figure 13.4 (a) Schematic diagram of two spheres contacting under normal force N . (b) Schematic diagram showing the rough contact interfaces between two pieces of conductive composites.

where ρ_b is the bulk resistivity, A is the (effective) contact area, and a is the radius of the circular contact. Tunneling resistance is associated with the tunneling current between the conductive fillers at the interfacial contact areas. The tunneling resistance is given as [87]:

$$R_t = \frac{\rho_t}{A} \tag{13.10}$$

where ρ_t is the tunneling resistivity, depending on the barrier thickness and barrier height by the following equation [89],

$$\rho_t = \frac{V}{J} \text{ and } J = \frac{e}{2\pi h \Delta s^2} \left[\begin{array}{c} \bar{\phi} \exp\left(-\frac{4\pi\Delta s\sqrt{2m}}{h}\sqrt{\bar{\phi}}\right) \\ -(\bar{\phi} + eV) \exp\left(-\frac{4\pi\Delta s\sqrt{2m}}{h}\sqrt{\bar{\phi} + eV}\right) \end{array} \right] \tag{13.11}$$

where V is the applied voltage, J is the current density, e is the elementary charge, h is Planck’s constant, Δs is the effective barrier thickness, $\bar{\phi}$ is the barrier height, and m is the electron mass.

Combining Eqs. (13.9), (13.10), and (13.11), the contact resistance R_c is

$$R_c = R_{cr} + R_t = \frac{\rho_b}{2} \left(\frac{\pi}{A}\right)^{1/2} + \frac{\rho_t}{A} \tag{13.12}$$

The contact resistance in Eq. (13.12) depends on the interfacial areas of the contact A , the resistivity of the bulk material ρ_b , and the tunneling resistivity ρ_t at the interfacial contact area. The contact areas of the system shown in Figure 13.4a can be analyzed using the Hertz normal contact theory [84], which gives the contact surface radius a and areas A under normal force F as follows,

$$a = \left(\frac{3Fr}{4K}\right)^{1/3} \text{ and } A = \pi a^2 = \pi \left(\frac{3Fr}{4K}\right)^{2/3} \tag{13.13}$$

where F is the normal force, K is the effective stiffness, and r is the effective radius of curvature of two spheres in contact.

The effective stiffness is given by

$$\frac{1}{K} = \frac{1 - \nu_1^2}{E_1} + \frac{1 - \nu_2^2}{E_2} \quad (13.14)$$

where E_1 and E_2 are Young's moduli and ν_1, ν_2 are the Poisson's ratios of the two spheres.

The effective radius is given by

$$\frac{1}{r} = \frac{1}{r_1} + \frac{1}{r_2} \quad (13.15)$$

where r_1 and r_2 are the radii of the two spheres.

Substituting Eq. (13.12) for A in Eq. (13.13) gives,

$$R_c = \frac{\rho_b}{2} \left(\frac{\pi}{\pi \left(\frac{3Fr}{4K} \right)^{\frac{2}{3}}} \right)^{1/2} + \frac{\rho_t}{\pi \left(\frac{3Fr}{4K} \right)^{\frac{2}{3}}} = \frac{\rho_b}{2} \left(\frac{4K}{3Fr} \right)^{\frac{1}{3}} + \frac{\rho_t}{\pi} \left(\frac{4K}{3Fr} \right)^{\frac{2}{3}} \quad (13.16)$$

If a bias voltage of V is applied, the current I is,

$$I = \frac{V}{R_c} = \frac{V}{\left(\frac{\rho_b}{2} \left(\frac{4K}{3Fr} \right)^{\frac{1}{3}} + \frac{\rho_t}{\pi} \left(\frac{4K}{3Fr} \right)^{\frac{2}{3}} \right)} \quad (13.17)$$

Equation (13.17) can be reduced to the following form if constriction resistance is dominant or tunneling resistance is dominant:

$$I \sim \begin{cases} \frac{2V}{\rho_b} \left(\frac{3Fr}{4K} \right)^{\frac{1}{3}}, & \text{if constriction resistance is dominant;} \\ \frac{\pi V}{\rho_t} \left(\frac{3Fr}{4K} \right)^{\frac{2}{3}}, & \text{if tunneling resistance is dominant.} \end{cases} \quad (13.18)$$

The sensitivity of the piezoresistive response of the contact resistance between two spheres can be estimated as:

$$S = \frac{d \left(\frac{\Delta R}{R_0} \right)}{dP} \approx \frac{d \left(\frac{R}{R_0} \right)}{dF} \sim \frac{1}{R_0} \left(\frac{\rho_b}{6} \left(\frac{4K}{3r} \right)^{\frac{1}{3}} \left(\frac{1}{F} \right)^{\frac{4}{3}} + \frac{2\rho_t}{3\pi} \left(\frac{4K}{3r} \right)^{\frac{2}{3}} \left(\frac{1}{F} \right)^{\frac{5}{3}} \right) \quad (13.19)$$

$$S = \frac{d \left(\frac{\Delta I}{I_0} \right)}{dP} \approx \frac{d \left(\frac{I}{I_0} \right)}{dF} \sim \begin{cases} \frac{2R_0}{3\rho_b} \left(\frac{3r}{4K} \right)^{\frac{1}{3}} \left(\frac{1}{F} \right)^{\frac{2}{3}}, & \text{if constriction resistance is dominant;} \\ \frac{2\pi R_0}{3\rho_t} \left(\frac{3r}{4K} \right)^{\frac{2}{3}} \left(\frac{1}{F} \right)^{\frac{1}{3}}, & \text{if tunneling resistance is dominant.} \end{cases} \quad (13.20)$$

The model aforementioned describes the piezoresistive response of two spheres in contact. For the device with arrays of spheres in contact, the equivalent circuit can be considered as the parallel contact resistor, which gives the device resistance as $R_{\text{device}} = R_c/N$, in which R_{device} is the device resistance, and N is the number of spheres in contact. The piezoresistive response of the device still follows the similar relationship described in Eqs. (13.16)–(13.20).

Assuming that ρ_b , and ρ_t are intrinsic material properties that do not change when the system is subjected to a normal pressure, the change of the contact resistance would be dominant by the change of the contact areas under pressure. This assumption is valid only for conductive elastomeric composites with conductive filler concentration well above the percolation threshold. In this case, the piezoresistive response is governed by Eq. (13.12) and is related to the pressure, the mechanical properties of the device, and the geometry of the device by Eqs. (13.13), (13.16), and (13.17). The sensitivity of the device, as shown in Eqs. (13.19) and (13.20), decreases with an increase in the applied pressure, following a negative power law relationship with applied pressure. The variation of the sensitivity (i.e. the linearity of the piezoresistive response) depends on the structure and stiffness of the device.

Both constriction resistance and tunneling resistance contribute to the contact resistance (Eq. (13.12)). As Eqs. (13.16) and (13.18) indicate, the constriction resistance and tunneling resistance follow the power law relationship of different exponent values with respect to pressure. The plot of $\log(R_c)$ versus $\log(P)$ may help understand the contribution of constriction resistance and tunneling resistance. In the composite composed of the conductive fillers embedded in a matrix, the size of the filler is typically much smaller than the contact area. Therefore, the constriction resistance is negligible, and the contact resistance is dominated by the tunneling resistance [87]. For the tunneling resistance, the material parameters essential to the tunneling current are the effective barrier thickness Δs and the barrier height $\bar{\phi}$, as indicated in Eq. (13.11). These parameters are related to the electrical properties of the filler, the distribution and concentration of fillers in the composite, and the interactions between the filler and matrix, which may be challenging to control precisely in composites.

The change of contact areas in the RTS based on the structural contact depends on the dimensions and shapes of the microstructure. For the two elastic spheres, the contact areas increase with the applied pressure and the radius of the sphere but decrease with the stiffness of the material, all following the 2/3 power law relationship. Different microstructures, such as hemispheres [89], micro-pyramids [74, 91], micro-pillars [92], hierarchical structures [93], and epidermis-inspired microstructures [94], have been explored for the RTS. While analytical models for the change of the contact areas in these microstructures under applied pressure may be challenging, finite-element simulations are routinely used to simulate and understand the mechanics of these microstructures under pressure.

Park et al. reported an RTS based on interlocked micro-domes (or hemispheres) arrays of carbon nanotube (CNT)/PDMS composite, as shown in Figure 13.5a(i). Finite-element analysis (FEA) was used to simulate the local stress and contact

areas under applied pressure. By varying the elastic modulus of composites with different CNT concentrations, the simulation results indicate that composites with low elastic moduli will undergo large deformation. The geometric contact area A_{dome} obtained by the simulation was refined to accurately represent the electrical contact area of CNTs, formulated as $A_{\text{CNT}} = \left(\frac{V_f}{2\pi}\right)^2$. Here, V_f symbolizes the volume fraction of the CNT in the composite and $\frac{V_f}{2\pi}$ represents the areal fraction in the cross-sectional area of the composite. Figure 13.5a(ii) plots the simulated A_{CNT} as a function of the applied pressure for composite with different CNT doping ratios. The result can be fitted with the power law function $y = ax^b$ with exponent $b = 0.7$ for all samples. The value is close to $2/3$ in Eq. (13.13), suggesting that the contact between the interlocked micro-domes is elastic within the simulated pressure range. The electric contact area increases with the increase of the fraction of CNT in the composite. For the device shown in Figure 13.5a(i), the tunneling resistance was calculated by $R_t = R_{\text{device}} - R_b$, omitting the constriction resistance. The tunneling resistance versus pressure can be fitted using Eq. (13.11), as shown in Figure 13.5b(viii). The fitting results reveal that the initial barrier thickness decreases with the increase of the fraction of CNT in the composite.

Pang et al. reported the RTS based on the epidermis microstructures of graphene/PDMS composite. The mechanism of the sensor is shown in Figure 13.5b(i–iii) [94]. The simulation of pressure distribution under 5 kPa pressure load for pyramid, hemisphere, nanowire, and randomly distributed spinosum (RDS) is visualized in Figure 13.5b(iv, v, vi, vii). Pyramid and hemisphere structures experience pressure concentration on the local contact area, leading to a pronounced increase in the contact area and heightened sensitivity at lower pressures, but this sensitivity sharply declines with increased pressure. The micro-pillar nanowire array has a uniform pressure distribution, while the RDS structure can transmit the concentrated stress at the peak to the root segment, thereby achieving a more homogenous pressure distribution. To further elucidate these observations, a MATLAB model was established incorporating the simulated contact areas and an equivalent circuit model of the parallel resistors in contacted structures. The resulting piezoresistive responses under pressure loading for different microstructures are shown in Figure 13.5b(viii). The results underscore an insight: randomly distributed microstructures can offer synergistic effects of high sensitivity and wider linear ranges for the RTS based on microstructured contact [94].

Ji et al. presented theoretical analysis and experimental design to optimize the sensitivity and linearity of RTS based on microstructured contact [86]. Figure 13.5c (i, ii, iii) shows the working principles of the piezoresistive response of the single conductive layer (SCL) devices composed of PDMS micro-domes spray-coated with carbon black PDMS (CPDMS) or dip-coated with silver nanowire (AgNW), and double conductive layer (DCL) device composed of PDMS micro-domes covered by both CPDMS and AgNWs double conductive layer (CPDMS/AgNWs DCL). Detailed theoretical analysis of these device structures reveals that the pass-through resistance (R_p in Figure 13.5c, denoted as orange resistors.) of the DCL structure balances the nonlinear variation in contact resistance under pressure, which contributes to

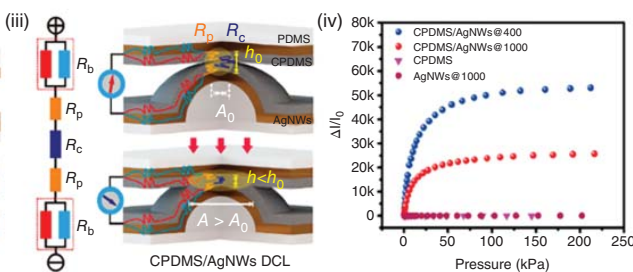
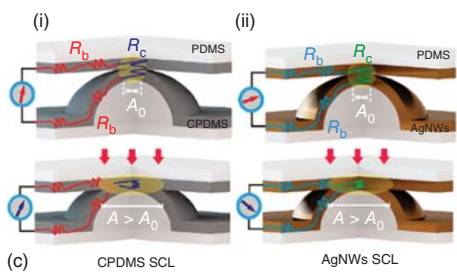
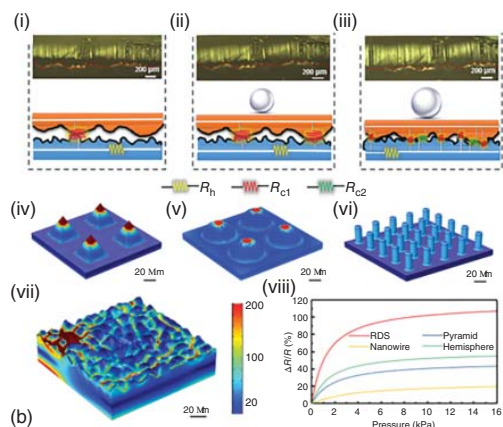
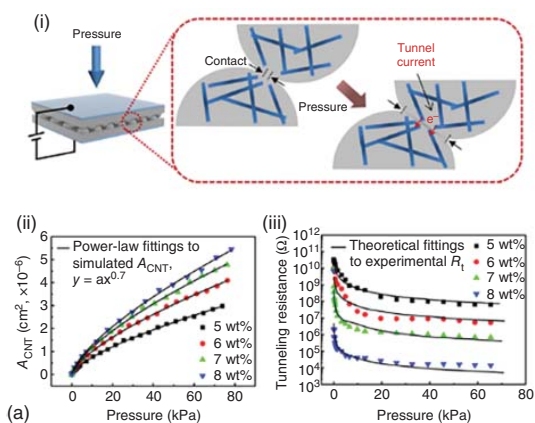


Figure 13.5 RTS based on microstructured contact. (a) (i) Schematic showing the working principle of the micro-dome-based RTS. (ii) The electrical contact area (A_{CNT}) as a function of pressure for different CNT wt% (5–8 wt%). A_{CNT} is estimated by considering the CNT area fraction over the geometrical contact area, which is obtained by using FEM simulation. The solid lines represent power law fits to A_{CNT} with an exponent of 0.7. (iii) Experimental tunneling resistances (dots) of the interlocked micro-dome arrays for different CNT concentrations (5–8 wt%) fitted to the tunneling resistance model (curves). Source: Reproduced with permission from Ref. [89]. Copyright 2014 American Chemical Society. (b) Working mechanism of the randomly distributed spinosum (RDS) graphene pressure sensor. Photographs and schematic illustrations of circuit models corresponding to (i) the initial state of unloading, (ii) light loading, and (iii) heavy loading. The pressure distribution of the simulation results for different geometries: (iv) pyramid, (v) hemisphere, (vi) nanowire, and (vii) RDS microstructure at an external loading pressure of 5 kPa. (viii) The simulation results of resistance variation versus applied pressure for different surface microstructures. Source: Reproduced with permission from Ref. [94]. Copyright 2018 American Chemical Society. (c) Schematic illustration of the principle of (i) CPDMS single conductive layer (SCL); (ii) AgNWs SCL, and (iii) CPDMS/AgNW double conductive layer (DCL); (iv) Relative current variation of the sensor fabricated with different conductive layers based on the solid dome array structure under external pressures. Source: Reproduced with permission from Ref. [86]. Copyright 2020 American Chemical Society.



highly sensitive and broad linear response (0 to 6 kPa) (Figure 13.5c(iv)) [86]. The device structure was further optimized by the synergistic effect of DCL and porous PDMS dome array.

13.2.3 Resistive Tactile Sensors Based on Bulk Conductive Nanocomposites

The piezoresistive properties of bulk nanocomposites, which are composed of elastomeric matrices and conductive fillers such as metal nanoparticles, graphenes, and CNTs, have been extensively investigated for their potential applications in tactile sensing [95]. Mechanisms of the piezoresistive properties of these materials are treated within the framework of percolation theory and an effective conductive path model in the literature. Figure 13.6 shows the schematic of several key aspects of the piezoresistivity of nanocomposites. The conductivity of the nanocomposite composed of conductive fillers depends critically on the concentration of the filler in the composite. Below the percolation threshold (insulation zone), the fillers cannot form a conductive path, and the nanocomposite has very low conductivity. The conductivity of the composite increases drastically when the filler concentration is around the percolation threshold (percolation zone), at which the conductive paths start to form; above the threshold (conduction zone), the conductivity continuously increases but with a small increment and eventually levels off. For the piezoresistive response, applied pressure may have a similar effect as the concentration of the conductive filler. Conductivity can increase drastically when the applied pressure leads to the formation of continuous conductive paths. Beyond the percolation concentration, the number of conductive paths can be described by the effective conductive path model. Additionally, the relaxation of the elastomeric matrices of the piezoresistive composite would affect the hysteresis, the response time,

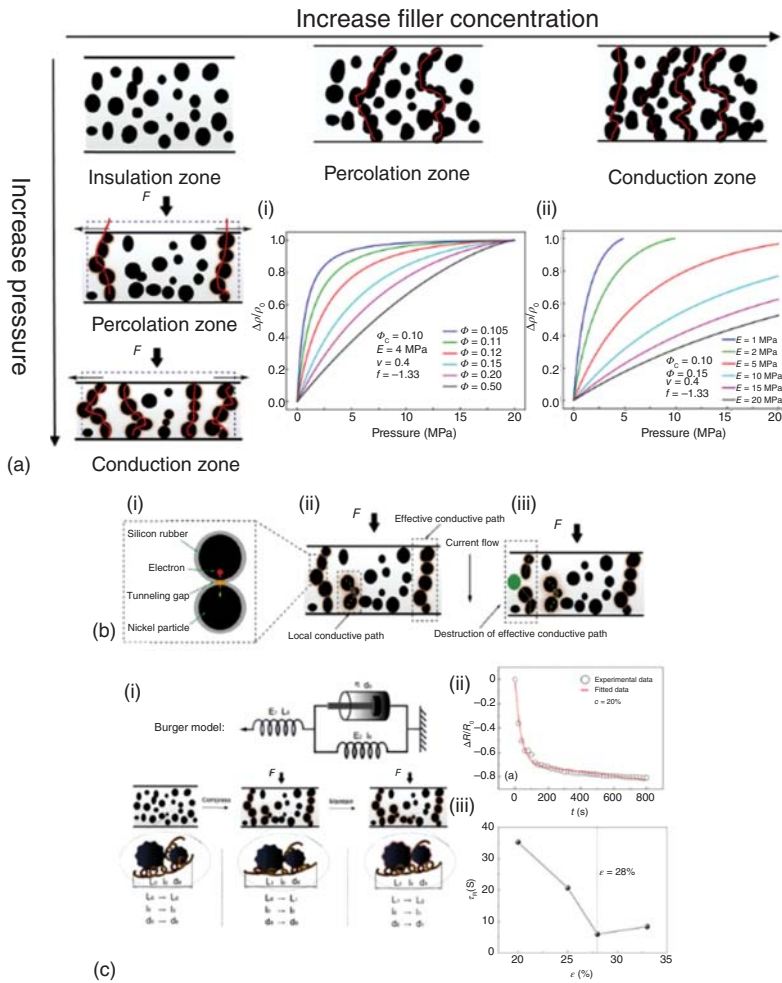


Figure 13.6 Percolation conduction mechanism. (a) Schematic diagram of the percolation conduction mechanism. Source: Reproduced with permission from Ref. [96]. Copyright 2017 Elsevier. (i) The relative resistivity change $\frac{\Delta R}{R_0}$, versus pressure for the composite with different filler volume fraction ϕ_0 calculated from Eq. (13.24) and assuming $\phi_c = 0.1$, $E = 4$ MPa, $\nu = 0.4$, and $f = -1.33$; (ii) $\frac{\Delta R}{R_0}$ versus pressure for the composite with different Young's moduli, calculated from Eq. (13.24) and assuming $\phi_c = 0.10$, $\phi_0 = 0.15$, $\nu = 0.4$, and $f = -1.33$. (b) Schematic diagram of effective conductive path model. (i) Tunneling through the thin film existing between the nearest metallic particles, (ii) formation of the effective conductive path, and (iii) destruction of the effective conductive path. Source: Reproduced with permission from Ref. [96]. Copyright 2017 Elsevier. (c) (i) Schematic diagrams of Burger's model and the change process of the microstructure of the percolation network for composites under static compression; (ii) Fractional electrical resistance change $\Delta R/R_0$ as a function of time t during stress relaxation at 20% strain for T4/123-4 FAQTC, "FAQTC" denotes the field-assisted quantum tunneling composites, "T4/123-4" represents the composite prepared by silicon T4 and type 123 spiky spherical nickel powders with a weight ratio of nickel powder to silicon rubber of 4 : 1 and cured; (iii) Fitted mean relaxation time as a function of strain. Source: Reproduced with permission from Ref. [96]. Copyright 2017 Elsevier.

and other aspects of the piezoresistive response. The piezoresistive responses of these materials can decrease or increase with applied pressure, depending on the material's composition, processing conditions, and other factors.

The resistivity of the nanocomposite can be described by the percolation scaling law [96],

$$\rho = X(\phi - \phi_c)^f \quad (\phi > \phi_c) \quad (13.21)$$

where ρ is the resistivity, X is the fitting constant, ϕ is the volume fraction of the conductive filler, ϕ_c is the percolation threshold volume fraction, and f is the percolation exponent. The value of f depends on the dimensionality of the filler. Note that the resistivity decreases with the increase of the conductive filler, so the value of f is negative. For 3D, $f = -2$ and for 2D, $f = -1.33$. Below ϕ_c , the composite can be considered as an insulator. Besides the volume fraction of the conductivity filler, the resistivity around the percolation threshold ϕ_c can change significantly by many other factors, including pressure, temperature (heating), and film thickness [97].

Assuming the nanocomposite is elastic under small uniaxial strain, the volume of the composite can be expressed by:

$$V_s = V_{s,0} \left(1 - \frac{P(1-2\nu)}{E} \right) \quad (13.22)$$

where V_s is the volume under pressure, $V_{s,0}$ is the initial volume, P is the applied pressure, ν is the Poisson's ratio, and E is the Young's modulus of the composite.

The filler volume fraction ϕ under pressure becomes

$$\phi = \frac{V_f}{V_s} = \frac{V_f}{V_{s,0} \left(1 - \frac{P(1-2\nu)}{E} \right)} = \frac{\phi_0}{1 - \frac{P(1-2\nu)}{E}} \quad (13.23)$$

where V_f is the volume of filler, ϕ_0 is the initial volume fraction of the conductive filler. Here, the filler is assumed to be incompressible so V_f is a constant under pressure.

Combining Eq. (13.22) and Eq. (13.23),

$$\frac{\Delta\rho}{\rho_0} = \frac{\rho_0 - \rho}{\rho_0} = 1 - \left(\frac{\frac{\phi_0}{1 - \frac{P(1-2\nu)}{E}} - \phi_c}{\phi_0 - \phi_c} \right)^f \quad (13.24)$$

where ρ is the resistivity under pressure, ρ_0 is the initial resistivity, and $\Delta\rho = \rho_0 - \rho$ is the change of the resistivity. The percolation threshold volume fraction ϕ_c is assumed to be unaffected by the pressure.

Equation (13.23) is only valid when the volume fraction is above ϕ_c . If the initial volume fraction is below ϕ_c , the resistivity of the nanocomposite does not change with the pressure until the percolation threshold pressure P_c is reached. P_c can be calculated by setting ϕ in Eq. (13.24) equal to ϕ_c .

$$P_c = \left(1 - \frac{\phi_0}{\phi_c} \right) \frac{E}{1-2\nu} \quad (13.25)$$

The piezoresistive response described in Eqs. (13.23) and (13.25) assumes the linear elasticity and small strain conditions. While the model may be oversimplified, it provides some insights into the piezoresistive response of the nanocomposite with conductive fillers.

- The composition of the nanocomposite is significant in determining the response of the RTS. In the scenario where the volume fraction of the conductive filler is lower than the percolation volume fraction, the resistivity of the sensor will remain unchanged until the pressure reaches the percolation threshold pressure P_c ; above P_c , the resistivity of the device can decrease significantly, resulting in a highly sensitive piezoresistive response. This behavior has been observed in spiky nickel nanoparticle-filled rubber composites [96]. For example, the electrical resistivity of a material composed of silicon T4 and nickel powders with a weight ratio of nickel powder to silicon rubber of 4 : 1 was above $10^9 \Omega \text{ cm}$; when the pressure was above 0.6 MPa, the resistivity dropped quickly by orders of magnitude. To utilize these materials in applications for tactile sensing, Eq. (13.24) suggests that the composition close to the percolation threshold concentration and with a low Young's modulus would lower the pressure detection limit of the device.
- The composition of the piezoresistive composite plays a crucial role in the tradeoff between the sensitivity and the detection range. Figure 13.6a(i) plots the relative resistivity change $\frac{\Delta\rho}{\rho_0}$ as a function of pressure for the composites with different filler volume fraction ϕ_0 , calculated from Eq. (13.22) and assuming $\phi_c = 0.1$, $E = 4 \text{ MPa}$, $\nu = 0.4$, and $f = -1.33$. When ϕ_0 approximated to ϕ_c , $\frac{\Delta\rho}{\rho_0}$ exhibits a rapid change at small pressure and then levels off, indicating high sensitivity and narrow operation range of the sensor. With a rise of the conductive filler concentration (i.e. increase of ϕ_0), the sensitivity decreases while the quasi-linear range becomes wider.
- Young's modulus of the piezoresistive composite is also linked to the tradeoff between the sensitivity and the upper detection range. Figure 13.6a(ii) plots the relative resistivity change $\frac{\Delta\rho}{\rho_0}$ versus pressure for the composites with different Young's modulus, derived from Eq. (13.22) and assuming $\phi_c = 0.10$, $\phi_0 = 0.15$, $\nu = 0.4$, and $f = -1.33$. The plot clearly indicates that a lower Young's modulus in the composite yields high sensitivity but restricts the working range. Conversely, a composite with a higher Young's modulus can function across a broader pressure range, albeit at a reduced sensitivity. Note that the pressure range of the plot is the result of $V_s = 0$ in Eq. (13.23) of the oversimplified elastic model and small strain assumptions, which are certainly not applicable for $V_s = 0$. Nevertheless, the result suggests controlling the Young's modulus of the composite may be important for optimization of the RTS based on the bulk conductive nanocomposites.

The resistivities of bulk conductive nanocomposites can be attributed to constriction resistance at the filler contact, tunneling resistance at the filler contact, and the intrinsic resistance of the filler [87]. Based on the model by Ruschau et al.

$$\rho_c^{\text{plastic}} = 0.89\rho_i \left(\frac{\lambda Hwt}{F} \right)^{\frac{1}{2}} + \frac{\rho_t \lambda Hwt}{Fd} + \frac{\rho_i}{0.524} \quad (13.26)$$

$$\rho_c^{\text{ceramic}} = 0.57\rho_i \left(\frac{Ewt}{F}\right)^{\frac{1}{3}} + \left(\frac{0.26\rho_t}{d}\right) \left(\frac{Ewt}{F}\right)^{\frac{2}{3}} + \frac{\rho_i}{0.524} \quad (13.27)$$

where ρ_c^{plastic} and ρ_c^{ceramic} represent resistivities of the composites with plastic fillers (polymer or metal) and ceramic fillers, respectively, ρ_i is the intrinsic resistivity of the filler, ρ_t is the tunneling resistivity, H denotes the contact hardness, and E represents Young's modulus of the composites, respectively, F is the applied force, w is the width of the composite, t is the thickness of the composite, d is the diameter of the filler, and λ is the empirical elasticity factor here.

The model anticipates that factors such as hardness, elastic modulus, filler particle size, and the overall dimensions of the composite sample significantly influence its piezoresistive properties. Specifically, fillers characterized by a higher modulus (or hardness) and smaller size are found to enhance the piezoresistivity of the composite. It is worth noting that Eq. (13.26) for the piezoresistive bulk nanocomposites and Eq. (13.16) for the contact-based RTS are essentially the same. In both models,

$$\rho_{\text{device}} \sim \left(\frac{1}{F}\right)^{\frac{1}{3}} \text{ for the constriction resistance} \quad (13.28)$$

$$\rho_{\text{device}} \sim \left(\frac{1}{F}\right)^{\frac{2}{3}} \text{ for the tunneling resistance} \quad (13.29)$$

Therefore, experimentally, the slope of the $\log(\rho_{\text{device}})$ versus $\log(F)$ plot may help understand the contribution of the constriction resistance and the tunneling resistance to the overall piezoresistive response.

In general, according to Eqs. (13.26) and (13.27), the tunneling resistance dominates the magnitude of the overall resistance of the composite. The effective conductive path model, which provides a microscopic conduction mechanism of the piezoresistive response of the bulk conductive nanocomposites [96, 98, 99], considers only the tunneling conduction in the composite. Figure 13.6b shows the schematic diagram of the effective conductive path. The model posits that applied pressure changes the distance between conductive fillers within the nanocomposite. A sufficiently reduced inter-filler distance enables electron tunneling between adjacent fillers, thereby establishing localized conductive connections. When these connections collectively form a continuous conductive pathway between electrodes through the matrix, the nanocomposite's resistivity decreases. Conversely, compressive forces may cause the fillers to slip, disrupting these effective conductive pathways and consequently increasing the resistivity. The nanocomposite's piezoresistive behavior emerges from the interplay of these two microscopic phenomena, quantifiable through the variation in the number of effective conductive paths during compression. The tunneling current between the two adjacent conductive particles is given by [98],

$$I^{ij} = \frac{3e^2 V^{ij} \sqrt{2m\phi^{ij}}}{2h^2 D^{ij}} \exp\left(-\frac{4\pi D^{ij} \sqrt{2m\phi^{ij}}}{h}\right) \quad (13.30)$$

where V^{ij} , ϕ^{ij} , D^{ij} are the external voltage, the height of the potential barrier, and the thickness of the insulating layer (i.e. tunneling gap in Figure 13.6b) between the

conductive filler i and j , m is the mass of electron, e is the elementary charge, and h is Planck's constant.

Then, the resistance of the i th effective conductive path can be given by considering the M_i number of conductive particles in series,

$$R_i = \sum_{j=1}^{M_i-1} R^{i,j} = \sum_{j=1}^{M_i-1} \frac{V^{i,j}}{I^{i,j}} = \sum_{j=1}^{M_i-1} \frac{2h^2 D^{i,j}}{3e^2 s^{i,j} \sqrt{2m\phi^{i,j}}} \exp\left(\frac{4\pi D^{i,j} \sqrt{2m\phi^{i,j}}}{h}\right) \quad (13.31)$$

where $s^{i,j}$ is the area of the cross-section of the insulating film between the conductive filler i and j .

To simplify the model, assuming the average insulating layer thickness D , the average number of conductive particles in one effective path M , the average cross-sectional area s , and the average barrier height ϕ , then Eq. (13.31) becomes:

$$R_i = (M - 1) \frac{2h^2 D}{3e^2 s \sqrt{2m\phi}} \exp\left(\frac{4\pi D \sqrt{2m\phi}}{h}\right) \quad (13.32)$$

The total resistance of the composite R can be calculated by considering the N effective conductive paths in parallel,

$$R = \frac{1}{N} \left[(M - 1) \frac{2h^2 D}{3e^2 S \sqrt{2m\phi}} \exp\left(\frac{4\pi D \sqrt{2m\phi}}{h}\right) \right] \quad (13.33)$$

In Eq. (13.33), the number of effective conductive paths N and the insulating film thickness between the fillers D depend on the applied pressure P . The change in the number of effective conductive paths, $\frac{N(P)}{N(P=0)}$, can be modeled using different empirical formulas [96, 98]. Ding et al. assumed that the number of the conductive paths increases exponentially with the applied pressure [96],

$$\begin{aligned} \frac{N(P)}{N(P=0)} &= \exp(A\epsilon + B\epsilon^2 + C\epsilon^3 + D\epsilon^4) \\ &= \exp\left(A\left(\frac{P}{E_c}\right) + B\left(\frac{P}{E_c}\right)^2 + C\left(\frac{P}{E_c}\right)^3 + D\left(\frac{P}{E_c}\right)^4\right) \end{aligned} \quad (13.34)$$

where $N(P)$ is the number of conductive paths under applied stress P , $N(P = 0)$ is the number of conductive paths with no stress, ϵ is the compressive strain, E_c is the compressive modulus of the composite, and A , B , C , and D are empirical parameters.

Assuming the conductive fillers are incompressible, the change in the insulating layer thickness between the adjacent conductive fillers under pressure can be expressed as follows:

$$\frac{D(P)}{D(P=0)} = (1 - \epsilon) = 1 - \frac{P}{E_c} \quad (13.35)$$

Combining Eqs. (13.34), (13.35), and (13.36), the ratio of resistance under pressure and no pressure can be expressed as

$$\frac{R(P)}{R(P=0)} = \left(1 - \frac{P}{E_c}\right) \exp\left(\left(A + \frac{4\pi\sqrt{2m\phi}}{h} D(\sigma=0)\right) \left(\frac{P}{E_c}\right) + B\left(\frac{P}{E_c}\right)^2 + C\left(\frac{P}{E_c}\right)^3 + D\left(\frac{P}{E_c}\right)^4\right) \quad (13.36)$$

Ding et al. fitted the piezoresistive response of nickel particle-filled elastomer composite using Eq. (13.36), giving a reasonably good agreement between the experimental data and the model. This model uses several fitting parameters, including A , B , C , and D in Eq. (13.36) and k_1 , k_2 , and k_3 for stress-dependent compressive modulus.

The model aforementioned posits an exponential increase in the number of conductive paths, as detailed in Eq. (13.34), leading to a monotonic decrease in resistivity with escalating compressive stress. Conversely, the applied compressive stress might also reduce the number of conductive paths owing to slippage and disconnection among adjacent filler particles, potentially elevating resistance [98, 100]. To account for these contrasting impacts of pressure on piezoresistive response, Wang et al. have delineated the relative alteration in the number of conductive paths with the subsequent equation [98],

$$\frac{N(P)}{N(P=0)} = \frac{1}{We^{-X \cdot P} + Ye^{Z \cdot P}} \quad (13.37)$$

where $W + Y = 1$, $W, X, Y, Z > 0$. In this case, the two terms in the denominator represent the two opposite effects of the pressure P on the number of conductive paths.

Combining Eqs. (13.33), (13.35), and (13.37), the ratio of resistance under pressure and no pressure can be expressed as

$$\frac{R(P)}{R(P=0)} = (We^{-X \cdot P} + Ye^{Z \cdot P}) \left(1 - \frac{P}{E_c}\right) e^{\left(\frac{4\pi\sqrt{2m\phi}}{h} D(P=0)\right)} \quad (13.38)$$

Since the distance between the adjacent filler particles, $D(P=0)$, can be correlated to the volume fraction and sizes of the filler particles in the composite, Eq. (13.38) serves as a model to elucidate the influence of various factors on the piezoresistive response of conductive nanocomposites. These factors include the volume fraction and size of the conductive filler, as well as the composite's compressive modulus. Wang et al. [98] successfully used Eq. (13.38) to interpret the diverse piezoresistive behaviors exhibited by silicon rubber infused with carbon black at varying concentrations. Their findings indicated that at low carbon black concentrations, resistance consistently decreases as pressure increases. In contrast, at moderate concentrations, resistance initially decreases and then rises with escalating pressure. Conversely, at high carbon black concentrations, the resistance consistently increases in response to rising pressure.

For RTS based on the bulk conductive nanocomposites, the matrix materials are typically elastomers (e.g. PDMS, silicon rubber, or polyurethane). These materials exhibit notable viscoelastic characteristics, including stress relaxation and creep, which can significantly influence the piezoresistive response of sensors incorporating conductive nanocomposites. A key challenge is that the piezoresistive response may change over time under constant strain or stress, leading to an inaccurate measurement in the practical application of these sensors. Despite its importance, such viscoelastic behavior has not been extensively explored in existing research [96, 101]. Ding et al. investigated the relaxation of the resistance of the nickel-particle-filled PDMS composite under stress [96]. Their experiments revealed that the composite's

resistance diminishes over time until reaching a steady state during stress relaxation. To model this phenomenon under pressure, the conventional Burger model was applied, as depicted in Figure 13.6c,

$$\frac{\Delta R}{R_0} = \frac{R - R_0}{R_0} = a + b \exp\left(-\frac{t}{\tau_R}\right) + ct \quad (13.39)$$

where R_0 denotes the initial resistance at time $t = 0$, R signifies the resistance at a subsequent time t , τ_R is the relaxation time, and a , b , and c are constants. Eq. (13.39) fits the resistance relaxation data at different strains well, as shown in Figure 13.6c(ii). The relaxation time τ_R of the device varies with the strain (Figure 13.6c(iii)), which is attributed to the rigid structure of the nickel particles.

In summary, the piezoresistive response of the RTS based on bulk conductive composites is modeled by percolation theory and an effective conductive path model. These models offer valuable insights into the underlying mechanisms governing the piezoresistive response. They highlight that filler concentration and composite modulus are critical parameters in the design of composite materials for RTS. However, the impact of stress relaxation on the piezoresistive response of these composite materials warrants further investigation, both theoretically and experimentally. Notably, current models, including the effective conductive path model, do not yet incorporate factors such as the influence of stress relaxation on the number of conductive paths and tunneling resistance, underscoring an area for future research and development.

13.2.4 Resistive Tactile Sensors Based on Porous Conductive Materials

The RTS based on porous conductive materials typically demonstrates a negative piezoresistive effect, characterized by a decrease in sensor resistance under compression. This behavior can be attributed to the formation of contact areas or points within porous material's structure under compression. Such compression facilitates the creation of additional conductive paths, consequently lowering the electrical resistance. Although this mechanism is widely accepted in the literature to elucidate the piezoresistive response of porous conductive materials, there is a scarcity of quantitative analyses that could offer practical guidance for the optimization of materials and structural designs specific to tactile sensors. This gap indicates a need for more detailed studies to inform and refine sensor design.

Highly porous materials exhibit hyper-elastic behavior. Their stress-strain response is characterized by the elastic, plateau, and densification regimes with an increase of the strain. The crucial parameters of a porous material are porosity (η), the relative density of the porous material (DP), and the density of the solid forming the porous material (d). Phenomenological models have been developed to understand the stress-strain response of the porous materials (such as polyurethane foams) and the effects of porosity, foam density, and loading rate [102]. These phenomenological models may be useful when the density and porosity of the porous conductive materials are considered for RTS applications.

Zhang et al. reported an analytical model of the piezoresistive behavior of highly compressible sensors made of microporous nanocomposites (Figure 13.7a)

[103]. In these materials, the porosity η decreases under applied stress/strain. The relationship between porosity and strain in highly porous materials may be complex. The complexity stems from predicting how porous materials will deform under compression. Such predictions are significantly influenced by both the porosity and the specific geometric characteristics of the porous materials. To offer a simplified model, the decrease in the porosity is assumed to be positively correlated with the deformation by $(1 - \eta) = (1 - \eta_0)/\lambda$, resulting in [103]:

$$\eta = 1 - \frac{(1 - \eta_0)}{\lambda} \quad (13.40)$$

where η is the porosity under compressive strain ε , η_0 is the original porosity, and λ is the stretch. Note that $\lambda = 1$ when the material is not under compressive strain and decreases with increase in the compressive strain/stress.

Following the highly compressible hyper-elastic model [106], the stress can be approximately correlated with the porosity η by the following equation:

$$\sigma = \frac{1}{\lambda} \sum_{i=1}^n \frac{2\mu_i}{\alpha_i} \left(\frac{1 - \eta}{1 - \eta_0} \right)^{\alpha_i} (\lambda^{\alpha_i} - 1) \quad (13.41)$$

where σ is the stress, n is the order of the model, and μ_i and α_i are the material parameters. The stress-strain curve of the carbon black/polyurethane (PU) porous nanocomposite (PNC) with different compositions and mechanical properties was fit to Eq. (13.41), and good agreement was obtained.

Following Archie's porosity-resistivity model [107], the conductivity of the porous conductive materials can be expressed as

$$k = k_0(1 - \eta)^f \quad (13.42)$$

where k is the conductivity of the porous material, k_0 is the conductivity of the solid that forms the porous material, and f is the exponent related to the microstructures of the pores.

Combining Eq. (13.40) and Eq. (13.42) leads to

$$k = \frac{k_0(1 - \eta_0)^f}{\lambda^f} \quad (13.43)$$

In the porous material based on the conductive filler/elastomer composite, quantum tunneling effects need to be considered when the material is compressed. A modified model can be written as:

$$k = \frac{k_0(1 - \eta_0)^f}{\lambda^a} \quad (13.44)$$

where a is a coefficient related to the microstructures, conductive fillers, and substrate material.

Equation (13.44) was used to fit the conductivity-porosity curve and conductivity-elongation curves of the porous composites with different contents of carbon black, as shown in Figure 13.7a(ii). The good fitting suggests that Eq. (13.44) can accurately represent the piezoresistive behaviors of highly porous medium. It is worth noting that the fitting parameters f and a are empirical, and the microstructure of

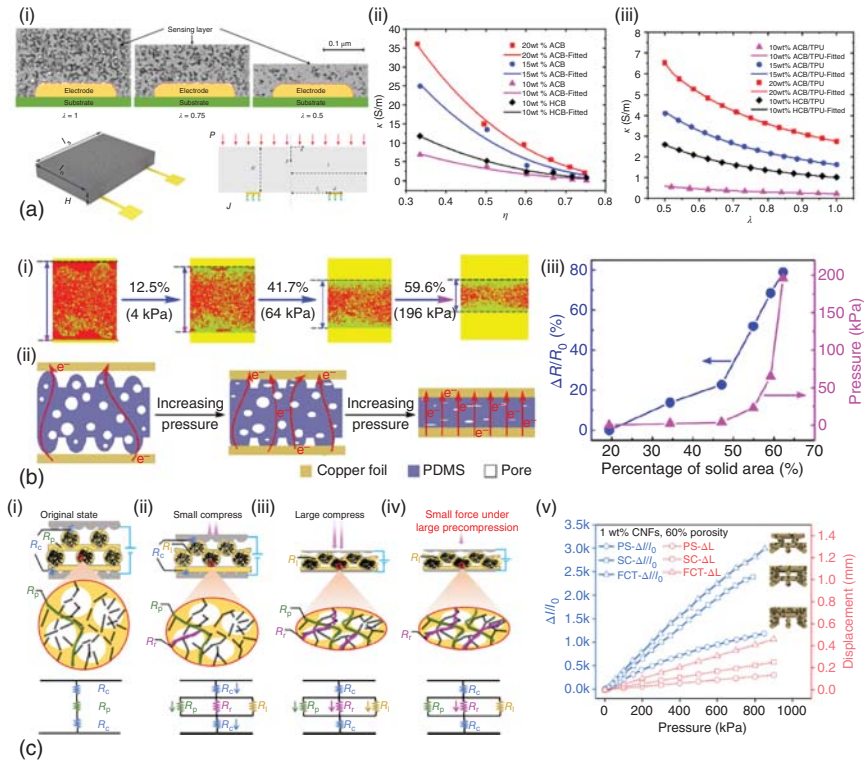


Figure 13.7 RTS based on porous conductive materials. (a) (i) The change of effective electric contact resistance at the microporous interface by pressing, schematic exploded view of a pressure sensor, and simplified 2D analytical model of the sensor; (ii) Conductivity–porosity curves of microporous nanocomposites with different contents of acetylene black (ACB) and highly conductive carbon black (HCB); (iii) Conductivity–elongation curves of microporous nanocomposites with different contents of ACB and HCB. Source: Reproduced with permission from Ref. [103]. Copyright 2021 John Wiley & Sons. (b) (i) Optical microscopic images acquired using an ultra-depth 3D microscope showing the cross-section of the sensor based on the B-micro/pore-3 structure under deformation. In the image, red, green, and yellow colors represent the pores, the solid PDMS region, and the metal holder, respectively; (ii) the proposed mechanism of the RTS based on the B-micro/pore-3 structure; (iii) pressure and $\Delta R/R_0$ (%) of the sensor under different percentages of solid area calculated from the cross-sectional images in Figure 13.7b(i). Source: Reproduced with permission from Ref. [104]. Copyright 2021 American Chemical Society. (c) Schematic illustration and circuit diagram of sensing mechanism of hierarchical porous piezoresistive sensor (i) in its original state, (ii) under small compression, (iii) under large compression. (iv) A tiny pressure change under a large preload is used to illustrate the high-pressure resolution performance; (v) Current response and sensitivity of 1 wt% carbon nanofibers, 60% porosity pressure sensor with different lattice structures (Parallel Stacked [PS], Simple cubic [SC], and Face-Centered Tetragonal [FCT]). Source: Reproduced with permission from Ref. [105]/Springer Nature/CC BY 4.0.

the porous material is missing. k_0 is related to the conductivity of the nonporous composite material.

Zhang et al. further treated the contact resistance at the microporous interface with electrode in terms of the equivalent contact area per unit area A_{ged} , porosity η_0 , and elongation λ . The contact resistance can be written as [103],

$$R_{\text{cr}} = \frac{\sqrt{\pi}\lambda^{a+b}}{4k_0(1-\eta_0)^{f-0.5}\sqrt{A_{\text{ged}}dW}} \quad (13.45)$$

where A_{ged} is the effective contact area per unit area, and d and W are the thickness and width of electrodes, respectively.

The contact resistance in Eq. (13.45) is similar to the constriction resistance in Eq. (13.9) but includes the parameters accounting for the porosity of the materials. Eq. (13.45) is useful for estimating the contribution of the contact resistance to the overall piezoresistive response of the porous conductive materials. While in most of the experimental studies of the piezoresistive porous materials, the contact resistance is not explicitly investigated, the change in the contact resistance can be significant due to the rough interface between the porous material and the electrode and may need more quantitative evaluation.

Analytical models of the microporous pressure sensor with a pair of electrodes or interdigitated electrodes were presented in Ref. [103]. Analytical solutions of the sensitivities to deformation and pressure were obtained and verified by the 3D FEA. The electromechanical behavior was simulated using the static thermomechanical modules because of the similarity between thermal governing equations and electrical governing equations. A scaling law for the device was also derived. These solutions were mathematically complex but provided a systematic analysis of the effect of the electrode configuration, the sensing layer dimension, and contact on the sensor performance. It is worth noting that the theoretical treatment here is for the co-planar electrodes and may not apply to the typical sensor configuration in which the two electrodes are on opposite sides of the sensing layer. The treatment also does not include many of the key parameters (e.g. pore size, density, concentration of filler, etc.) of the porous materials that govern the hyper-elastic mechanical properties.

One of the strategies to improve the sensitivity and detection range is to design a piezoresistive material combining the contact microstructures and the porous materials. Such porous material is based on patterning surface microstructures on the PDMS/MWCNT (multiple wall carbon nanotubes) porous structure by nonwoven fabric [104]. As a result of the synergistic interaction between the porous structure and surface microstructure, the flexible sensor exhibited a highly sensitive piezoresistive behavior across a broad pressure range from 1 Pa to 100 kPa. The high sensitivity at lower pressure was attributed to changes in the contact areas between the electrodes and surface microstructures. At higher pressure, up to 100 kPa, the sensor maintained its sensitivity, primarily due to the inherent porous nature of the piezoresistive PDMS/MWCNT material. As shown in Figure 13.7b, the mechanism was in general described as an increase of conductive paths under applied pressure. To better understand the sensing mechanism and the effects of porosity/contact,

the cross-sectional images of the sensor under pressure were collected by an ultra-depth three-dimensional microscope, and then the percentage of the solid component in the image was calculated as the percentage of solid area in the image. Figure 13.7b(iii) shows the relative resistance change or pressure as a function of the percentage of the solid area. The result provides the direct experimental data of the porosity change with the piezoresistive response or pressure, which may be useful for future correlation of the experimental material design and theoretical modeling of the RTS.

Xu et al. recently reported an innovative approach to fabricate piezoresistive pressure sensors with high sensitivity and broad linearity range [105]. A hierarchical in situ filling porous structure as the sensing layer was fabricated by direct writing printing and curing of carbon nanofibers (CNFs)/PDMS emulsion. First, the emulsified water droplets filled with CNFs were dispersed in the PDMS emulsion. The CNFs/water/PDMS emulsion could be extruded uniformly and continuously and stacked layer-by-layer to form a 3D lattice structure. After curing the PDMS, water evaporated, and left pores filled with CNFs. Compared with the conventional porous conductive materials, in which the conductive fillers are only in the solid and the edge of the pore, the unique fabrication process ensures that the conductive fillers not only adhere to the edges of the pores but also fill the pores *in situ*. Figure 13.7c(i) shows the relative change of the current as a function of pressure for four types of sensing layers of 1 wt% CNFs and 60% porosity. The synergetic effect of the internal CNF-filled pores and the lattice structure results in the device with the highest sensitivity of 2.4 kPa^{-1} and a high linearity ($R^2 = 0.993$) up to 1 MPa. Different porosities, concentrations of CNFs, and lattice structures were also investigated. The mechanism of the improved sensing performance is schematically described in Figure 13.7c(ii). Under compression, the lattice structure can readily deform, resulting in large contact area changes, effective stress distribution, and generating more conductive paths. When subjected to slight pressure changes, the CNF networks embedded within the internal porous structure can easily establish contact with each other, creating freestanding conductive paths within the internal pores. Moreover, the CNF networks act as a “bridge,” connecting the isolated conductive fillers dispersed at the pore edges and forming additional conductive paths. This results in the generation of conductive paths within the elastomer, pores, and elastomer-pore interface. Consequently, a more substantial resistance change can be induced across the entire sensing range.

New strategies for achieving high sensitivity and wide-linear range RTS have rapidly evolved in recent years [108–110]. Chen et al. reported using an elastic spacer surrounding the sensing layer to improve the sensitivity of an RTS over a wide linear range (up to 1.4 MPa) [108]. By introducing the stiffness control of the elastic spacer, effect of micro-pyramid geometry on the sensitivity can be canceled by the stiffening constant, resulting in a wide linear range of the sensor. In a different approach, a broad linear range and highly sensitive pressure sensor were achieved by the design of multigradient materials (including modulus, conductivity, and microstructure gradient) [110]. Fine control of the mechanical and structural properties of piezoresistive sensing materials and devices will need to have better

analytical and numerical models for devices with high sensitivity and linearity over a wide pressure range for future applications in e-skins and other practical applications.

13.2.5 Stretchable Resistive Tactile Sensors

Most studies on flexible RTS based on soft conductive materials do not consider how to decouple the response of the devices induced by pressure or lateral stretch. Research on stretchable RTS is still at an early stage [111–113]. To incorporate stretchability into the RTS, strategies for stretchable conductive pressure-sensing material, stretchable electrodes, and stretchable structural engineering have been proposed. Several examples of stretch-insensitive RTS are discussed in this section. This section begins by introducing how to mathematically quantify “strain insensitivity” [114], followed by strategies to mitigate stretch interference. The term “strain insensitivity” was first introduced in Ref. [114], herein, we further refine the mathematical definition of “strain insensitivity”.

As illustrated in Figure 13.2b, lateral stretch geometrically affects both the area and the thickness of an RTS, resulting in a change in the resistance according to Eq. (13.1). Figure 13.8a offers an example [113]: the resistance at 10 kPa pressure and a concurrent 50% uniaxial strain, marked by the yellow triangle, is much higher than the resistance at the same pressure without any lateral strain, indicated by the yellow square. This lateral-stretch-induced offset in resistance would result in unreliable pressure measurement when both pressure and stretch are present. To quantitatively evaluate stretch interference, Figure 13.8b presents a plot prepared by us. In this plot, resistances without lateral strain and with 50% uniaxial strain from Figure 13.8a are plotted as the x-axis and y-axis, respectively. If the RTS is completely stretch insensitive, then the experimental results should all fall on the diagonal dash-dot line represented by $y = x$. However, the stretch interference causes the actual data points

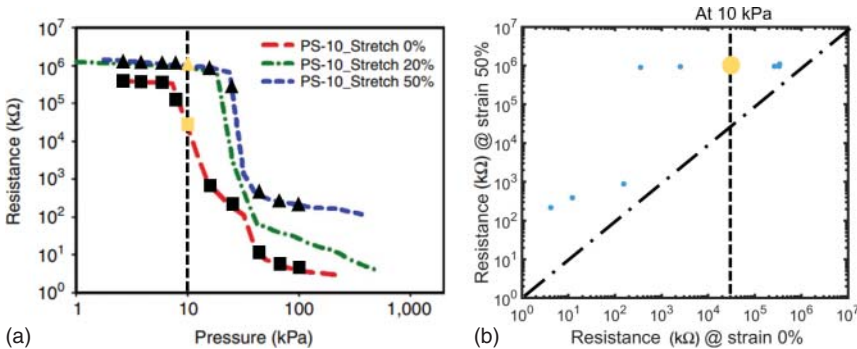


Figure 13.8 Definition of strain insensitivity. (a) The resistance change of an RTS under pressure without strain (red), under pressure (green) and concurrent 20% (green) or 50% (blue) uniaxial strain. Source: Adapted from Ref. [113]. (b) Resistive response under both pressure and 50% uniaxial strain versus resistive response under only pressure. Markers closer to the dash-dotted line indicate higher strain insensitivity.

to deviate from this line, as illustrated by the blue markers in the graph. To quantify this deviation, we apply two statistical metrics: the root mean square error (RMSE)

$$\text{RMSE} = \sqrt{\frac{\sum_{i=1}^n (R_{P+S}^i - R_p^i)^2}{n}} \quad (13.46)$$

Here R_{P+S}^i is the resistance under concurrent pressure and stretch for the i th observation in the dataset, and R_p^i is the resistance under only pressure for the i th observation in the dataset. n is the sample size of the experiment data set, which equals 10 in the experimental data given in Figure 13.8a. The normalized root mean square error (NRMSE):

$$\text{NRMSE} = \text{RMSE} / \bar{R}_{P+S} \quad (13.47)$$

The average resistance under both pressure and stretch conditions, denoted as \bar{R}_{P+S} , is calculated as $\bar{R}_{P+S} = \frac{\sum_{i=1}^n R_{P+S}^i}{n}$. The NRMSE is a statistical metric that ranges from 0 to infinity, providing insight into the stretch insensitivity. Specifically, an NRMSE value greater than 1 signifies a substantial discrepancy between R_{P+S}^i and R_p^i , indicating significant stretch interference. An NRMSE between 0 and 1 suggests some degree of stretch interference, but not overwhelmingly so. When NRMSE is 0, it indicates that stretch does not introduce any interference into the measurement. This scenario represents an ideal situation for stretch-insensitive tactile sensors.

In this framework, strain insensitivity is defined as $1 - \text{NRMSE}$. A strain insensitivity value below 0 implies that the tactile sensors are severely compromised in their ability to accurately measure pressure when subjected to stretch. On the other hand, a value approaching 1 indicates a high level of strain insensitivity, meaning the sensor's performance is minimally affected by stretch. Referring back to our example, the strain insensitivity index based on Figure 13.8b [113] is -2.13 , indicating a significant stretch interference of resistance reading. Consequently, the sensors in Ref. [113] are deemed incapable of providing accurate readings under simultaneous pressure and stretch conditions.

Before the recent proposal of the metric of strain insensitivity for quantifying stretch interference, several strategies were developed to mitigate the issue of stretch interference. One approach involved spacers, as illustrated in Figure 13.9a(i), in which the RTS consists of four components [115]: the Ecoflex matrix, the PDMS spacer, and the top and bottom electrodes, along with the porous sensing materials. The relatively stiff PDMS spacer insulates against in-plane strain, while the soft Ecoflex matrix exhibited significant deformation. This design effectively isolated strain in both the x and y directions, resulting in resistive responses under concurrent pressure and stretch that closely resembled the response of sensors subjected only to pressure (Figure 13.9a(ii)). Figure 13.9b(i) introduces another strategy known as fabric RTS [112]. These sensors are composed of conductive fibers (depicted as the red helices in Figure 13.9b(ii)) wrapped around nonconductive fibers (yellow strands), creating a fabric-like structure. When the sensor is stretched, the contacts between conductive fibers remain more or less unchanged, whereas new contact points form under compression. As a result, its stretch insensitivity was found to be 0.99.

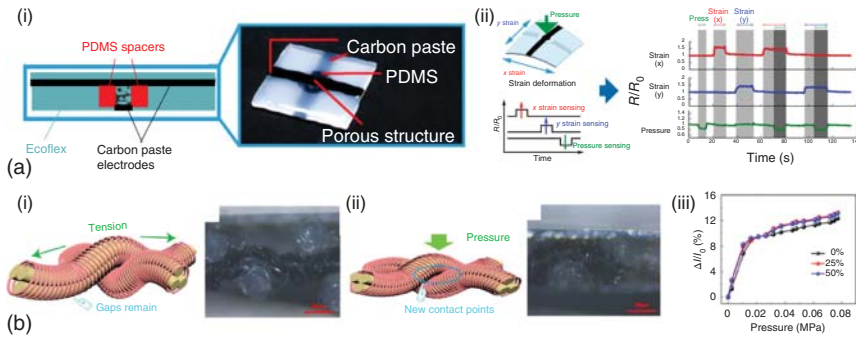


Figure 13.9 Strategies for reducing the stretch interference in resistive pressure sensors. (a) (i) Illustration of the spacer design of RTS. (ii) The normalized resistance versus pressure under spontaneous stretches along different directions. Source: Reproduced with permission from Ref. [115]/Springer Nature/CC BY 4.0. (b) Fabric design of RTS under stretch (left) (i) and pressure (ii); (iii) The normalized current change versus pressure under no stretch (black) and spontaneous 25% (red) and 50% (blue) uniaxial stretch. Source: Reproduced with permission from Ref. [112]. Copyright 2020 American Chemical Society.

To provide a comprehensive comparison, Table 13.2 summarizes several representative stretchable RTS in terms of sensing mechanism, sensor structure, material, sensitivity, pressure range, and calculated strain insensitivity. This analysis reveals a notable gap: a sensor that simultaneously exhibits high sensitivity and high strain insensitivity is yet to be developed. This highlights the ongoing challenge in sensor technology to create devices that can accurately measure pressure without being influenced by external factors like stretching.

13.3 Capacitive Tactile Sensors

13.3.1 Introduction of Capacitive Tactile Sensors

Conventional flexible CTS are formed by sandwiching a mechanically compliant dielectric layer between two thin electrodes, as depicted in Figure 13.10a. The corresponding circuit is just a simple capacitor (Figure 13.10b), where the capacitance C can be expressed as:

$$C = k\epsilon_0 \frac{A}{d} \quad (13.48)$$

where k is the dielectric constant of the dielectric, which is a measure of a material's response to an electric field, ϵ_0 is the permittivity of vacuum, A is the area of the electrodes, and d is the gap in between.

Upon compression, the electrode gap shrinks, but the electrode area does not change. Therefore, the relative change in capacitance is

$$\frac{\Delta C}{C_0} = \frac{k}{k_0} \frac{d_0}{d} - 1 \quad (13.49)$$

Table 13.2 Summary of Representative Flexible and Stretchable RTS.

References	Structure	Material	Mechanism	Sensitivity (kPa^{-1}) (Sensing range [kPa])	Stretch insensitivity (stretchability)
[112]	Fabric	Resistive rubber	Contact resistance	~ 0.008 (0–10) ~ 0.001 (10–80)	0.952 (50%)
[60]	Film	PVDF/ Ti_3AlC_2	Contact resistance	~ 817.4 (0.072–0.74) ~ 2213.3 (0.74–3)	NM
[69]	Micro-domes	CNT/PDMS	Tunneling resistance/ contact resistance	~ 15.1 (0–0.5) ~ 1000 (0.5–2.5)* ~ 0.1 (2.5–30)*	NM
[116]	Micro-domes	AgNW/ PDMS	Contact resistance	~ 3 (0–2.5)* ~ 0.33 (2.5–22.5)*	0.394 (100%)
[74]	Micro-pyramids	PEDOT: PSS/PUD	Contact resistance	~ 4.88 (0–3) ~ 1.54 (3–8)	0.537 (40%)
[113]	Micro-pyramids	SWCNT	Contact resistance	~ 0.75 (0–11)* ~ 134 (11–100)*	–0.105 (50%)
[111]	Micro-pyramids	AgNF/ graphene	Contact resistance	~ 1.6 (0–200)*	–2.13 (50%)
[117]	Sponge	CNF/ PAN/PI NF	Porous structure contact	~ 84.9 (0.05–5) ~ 140.9 (6–22)	NM
[118]	Sponge	Chitosan/ MXene/PU	Contact resistance/ interior contact	~ 147 (0–5) ~ 442 (5–17)	NM
[98]	Sponge	MXene	Porous structure contact	~ 0.1 (0–15)	NM
[115]	Porous structure	CNT/PDMS	Porous structure contact or contact resistance (not clearly stated)	~ 1.6 (0–5) ~ 0.2 (5–25)	0.99 (50%)
[83]	Tetragonal structure	CNF/PDMS	Porous structure contact	~ 4.7 (0–1000)	NM

“PVDF” denotes polyvinylidene fluoride. “CNT” denotes carbon nanotubes. “PEDOT:PSS” denotes poly(3,4-ethylenedioxythiophene) polystyrene sulfonate. “PUD” denotes aqueous polyurethane dispersion. “AgNF” denotes silver nanofiber. “CNF” denotes carbon nanofiber. “PAN” denotes polyacrylonitrile. “PI NF” denotes polyimide nanofiber. “PU” denotes polyurethane. The * denotes the sensitivity determined using a two-point slope within the corresponding sensing range. “NM” indicates “not mentioned.”

Source: Refs. [73, 74, 89, 105, 111–113, 115–119].

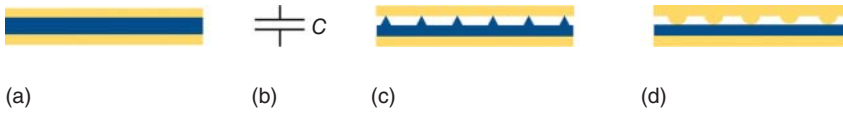


Figure 13.10 Schematics of representative types of CTS. (a) Flat electrodes sandwiching a solid dielectric layer. (b) The circuit model of CTS. (c) CTS with engineered dielectrics. (d) CTS with engineered electrodes.

The initial sensitivity S is therefore

$$S = \frac{d\left(\frac{\Delta C}{C_0}\right)}{dP} = \frac{1}{E_0} + \frac{1}{k_0} \frac{\partial k}{\partial P} \quad (13.50)$$

This equation indicates that the initial sensitivity of CTS can be enhanced through two primary strategies:

- **Employing a soft dielectric layer.** This method suggests choosing a dielectric material with a lower effective Young's modulus (E), as it could facilitate a greater decrease in the distance “ d ” with the same amount of pressure applied.
- **Leveraging the dielectrostriction effect.** Dielectrostriction is a phenomenon that describes how the effective dielectric constant changes under pressure, denoted as a nonzero value of “ $\partial k/\partial P$ ” [120]. A good example to illustrate this is a porous material filled with a combination of high- k material and air. As the material gets compressed, the air is replaced with more of the high- k material, resulting in an increase in the overall effective dielectric constant.

Building on these observations, extensive research has focused on improving the structure, mechanical characteristics, and electrical attributes of dielectrics. These efforts have ushered in what we term “engineered dielectrics,” as depicted in Figure 13.10c. In addition, “engineered electrodes,” shown in Figure 13.10d, have also been investigated. This section provides a summary of the established electromechanical understandings related to “engineered dielectrics” and “engineered electrodes.”

13.3.2 Capacitive Tactile Sensors with Engineered Dielectrics

CTS with micro-patterned dielectrics is sensitive within subtle and low-pressure regimes with a fast response time. Mannsfeld et al. first introduced micro-patterned CTS in 2010 [44]. Micro-pyramid dielectric patterns are fabricated by casting PDMS onto a pyramid silicon mold. The dielectric micro-pyramids enabled CTS to achieve a sensitivity of 0.55 kPa^{-1} within the 0–7 kPa pressure range, with swift recovery times measured to be just a few dozen milliseconds – 30 times faster than CTS with solid dielectrics.

To improve the sensitivity, micro-patterned structures, including micro-pyramids [123], micro-domes [124], and micro-pillars [125], have been designed to consider various geometric parameters, such as sizes, shapes, and spacing between microstructures. Finite-element modeling (FEM) [123, 126] has been employed

to optimize sensor sensitivity. FEM allows for the computational simulation and analysis of the physical behavior of these sensors, thereby reducing the reliance on physical experiments for optimization. It provides a means to virtually experiment with different design parameters, such as base length, geometry height, and other structural aspects of micro-patterns like micro-pyramids. While FEM is available for understanding and predicting the performance of specific structures like micro-pyramids, it typically allows only limited explorations of sensor performance by adjusting structural parameters of a specific structure like micro-pyramids. One of the limitations of this approach is that the crucial design parameters for a broad range of applications are not always identified. In addition, even if some crucial design parameters are identified in FEM, it is not clear for scientists to know how crucial design parameters influence sensor performance. These gaps in the methodology restrict the widespread applicability of FEM in the design of CTS.

To overcome the limitations of FEM in the design and optimization of CTS, theoretical models of CTS have been explored. One such approach is seen in the work of Sara et al., who introduced a comprehensive model for microstructured CTS [39]. This model systematically investigated sensor performances by varying structural and material parameters, offering a more holistic understanding of how different design choices impact sensor functionality. The capacitance of these micro-patterned CTS can be calculated using the equivalent circuit illustrated in Figure 13.11b(i):

$$C = \frac{C_{\text{air}} C_{\text{pyramid}}}{C_{\text{air}} + C_{\text{pyramid}}} \quad (13.51)$$

where capacitances of each component are defined as:

$$C_{\text{air}} = \frac{f_{\text{air}} A \epsilon_{\text{air}}}{t_{\text{pyramids}}}, C_{\text{pyramids}} = \frac{f_{\text{p}} A \epsilon_{\text{pyramids}}}{t_{\text{pyramids}}} \quad (13.52)$$

Here, the f_{air} represents the volumetric fraction of air, while f_{p} represents volumetric fraction of pyramids,

Upon compression, the dielectric materials are highly simplified as a spring with their stiffness k :

$$k = \frac{EA}{t} \quad (13.53)$$

where E is the dielectric material's modulus, A is the contact area between the electrode and pyramid, and t is the total height of the pyramid as illustrated in Figure 13.12b(ii). It is assumed to have a small pressure range so that the volumetric fraction and the shape change of microstructures are negligible. According to Hook's law, $F = kx$, where F is the applied force and x is the deflection. Rearranging Eq. (13.53), the deflection is expressed as

$$x = \frac{Ft}{EA} \quad (13.54)$$

Using known geometric relationships of trapezoids, the effective $1/A$ for micro-pyramids is expressed:

$$\frac{1}{A} = \int_0^t \frac{t}{(ad - a\delta + b\delta)^2} d\delta \quad (13.55)$$

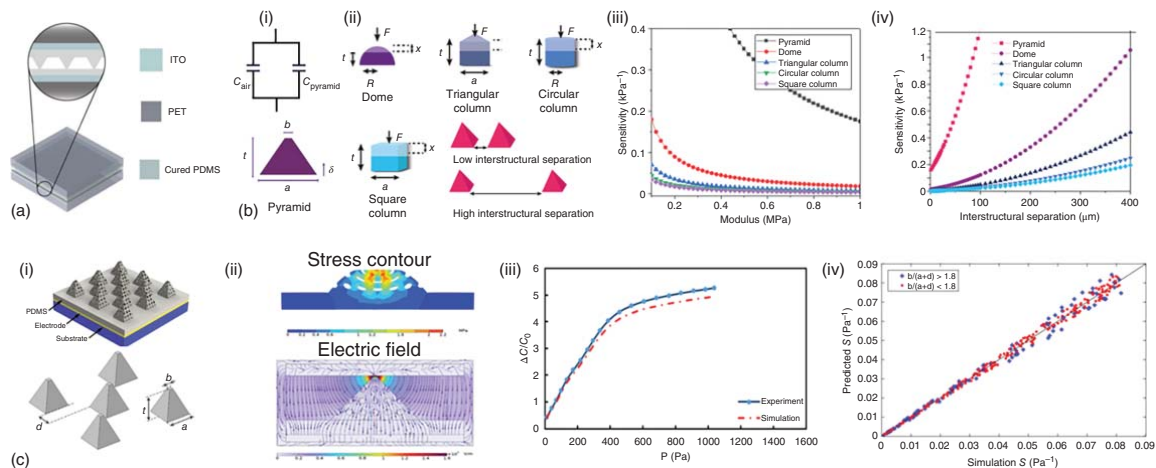


Figure 13.11 CTS with micro-patterned dielectrics. (a) Schematics of CTS with micro-pyramids patterned on the surface of the dielectric. Source: Reproduced with permission from Ref. [39]. Copyright 2019 Wiley. (b) (i) Equivalent circuit of micro-pyramid CTS (top) and design parameters of the pyramids (bottom). Source: Reproduced with permission from Ref. [39]. Copyright 2019 John Wiley & Sons. (ii) Schematics of other surface micro-patterns. The dependence of sensitivity on the (iii) dielectric modulus and (iv) interstructural separation. Source: Reproduced with permission from Ref. [121]. Copyright 2020 American Chemical Society. (c) (i) CTS with porous micro-pyramids. (ii) The stress distribution (top) and the electrical field distribution in the porous micro-pyramid under compression. (iii) Comparison of the relative change in capacitance between simulation and experimental results. (iv) The predicted sensitivity versus the simulated sensitivity. Source: Reproduced with permission from Ref. [122]/Springer Nature/CC BY 4.0.

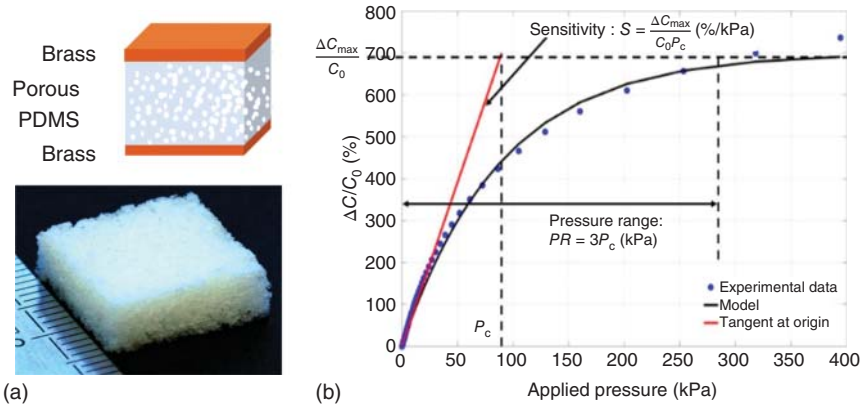


Figure 13.12 CTS with foam dielectrics. (a) Schematics of CTS with foam dielectrics (top) and a photograph of the foam (bottom). (b) An empirical model for the relative capacitance changes versus pressure. Source: Reproduced with permission from Ref. [127]/MDPI/CY BY 4.0.

where δ is the distance from each layer to the bottom, a is base length of pyramids, and t is the height of pyramids. Combining Eqs. (13.54) and (13.55) gives us:

$$x = \frac{F}{E} \int_0^t \frac{t^2}{(ad - a\delta + b\delta)^2} d\delta \tag{13.56}$$

This analytical expression matches well with the experiment results for micro-pyramid dielectric CTS [39]. Subsequently, Sara et al. expanded this expression to other micro-patterned sensors by substituting different effective $1/A$ for domes, triangular columns, circular columns, and square columns [121] (as depicted in Figure 13.11b(ii)). In the study, a pressure of 1 Pa and the corresponding applied force on sensor F were utilized to update the deflection x according to Eq. (13.54) followed by calculation of the capacitance change based on Eqs. (13.51) and (13.52) and sensitivity.

To identify the crucial design parameter, Sara et al. systematically varied parameters, such as dielectric materials’ modulus E , dielectric constant k , base length a , height t , and interstructural separation for five different structures through theoretical modeling (Figure 13.11b(ii)). An important aspect of their study is the consideration of different effective $1/A$ values and varying volumetric fractions of air for each structure. According to their investigation, modulus E and interstructural separation are two crucial factors for sensitivity enhancement (Figure 13.11b(iii,iv)).

For all five structures, amplifying the modulus of dielectrics by an order of magnitude consistently led to a roughly equivalent decrease in initial sensitivity, as depicted in Figure 13.11b(iii). An enhancement of interstructural separation boosts sensitivity (Figure 13.11b(iv)), which effectively diminishes the volumetric ratio of dielectrics, consequently reducing initial capacitance while augmenting the volumetric ratio of air. Remarkably, compared with other structures, the pyramid and dome configurations stand out. This superior performance is largely ascribed to their comparatively lower initial modulus (Figure 13.11b(iii,iv)) [121].

The impact of the dielectric constant on sensitivity is markedly overshadowed by Young's modulus and interstructural separation. An increase in the dielectric constant k from 1 to 60 results in only a modest enhancement of sensitivity from 4 to 11 kPa⁻¹ (Ref. [121]). It was also found that enlarging the base length or diameter of microstructure (dome, triangular, circular, and square column) led to a decline in the sensitivity, while this trend has only been demonstrated experimentally with the dome structures [128] and using FEM for the circular columns [129]. Base length and height also contributed to the sensitivity. An increase in base length leads to reduced sensitivity across all structures due to the resultant higher volumetric ratio of dielectrics. In contrast, for triangular, circular, and square column structures, an increase in height correlates with enhanced sensitivity, since increase in height indicates a larger increase in distance between two electrodes [129]. Additionally, it was discerned that comparable changes in the base length and height yield similar effects on sensitivity change. Yet, in contrast to Young's modulus, these dimensions exert a relatively minor influence on sensitivity. This revelation is pivotal for sensor design, underscoring that mere alterations in structural dimensions fail to significantly boost sensitivity and are limited by the constraints of molding techniques. Therefore, the research focus should pivot toward a more profound exploration and refinement of the materials used in CTS.

In addition to the theoretical model for solid micro-patterns offered by Sara et al., Reza et al. proposed porous micro-pyramids for CTS using FEM to simulate electromechanical behaviors (Figure 13.11c(i)) [122]. This design includes several key dimensions: d is the interstructural separation, t is the height of the pyramid, a is the length of the pyramid base, and b is the length of the top of the pyramid. Subsequently, the Neo-Hookean model was employed to describe the mechanical behavior of the dielectrics:

$$W = C_{10}(I_1 - 3) \quad (13.57)$$

where C_{10} is the material constant and I_1 is the first invariant of the left Cauchy-Green deformation tensor. By applying pressure on the top electrodes, the deformation and stress contour can be illustrated in Figure 13.11c(ii). The governing equations for the electric field in the CTS can be described by Gauss's law,

$$\nabla \cdot (k\epsilon_0 \nabla V) = \rho_v \quad (13.58)$$

where k represents the relative dielectric constant of the domain, V represents the electric potential field, ρ_v represents the volumetric free charge density, and ϵ_0 is the permittivity of vacuum. The electrical field \vec{E} can be expressed as:

$$\vec{E} = -\nabla V \quad (13.59)$$

Therefore, the electric field can be observed in Figure 13.12c(ii). The electrical simulation results showed strong alignment with the experimental data, as depicted in Figure 13.12c(iii), demonstrating the accuracy of their FEM. Having confirmed the validity of FEM, the author generates a sensitivity FEM dataset by varying sensor parameters such as base height, interstructural separation, and porosity [122]. Subsequently, all of the dataset points are fitted to a theoretical relationship. The original

expression, which is too complex to be presented here, is replaced with a simplified coefficient multiplied by a function f for explanatory purposes:

$$S \sim \frac{(1 + d/a)^2}{\nu \left(\frac{b}{a}\right) E} f\left(\frac{d}{a}, k, \frac{b}{a}\right) \quad (13.60)$$

where δ symbolizes the porosity of the dielectric layer. As illustrated in Figure 13.12c(iv), the simulated values for S closely aligned with the predicted values presented in the paper. Furthermore, $S \sim \frac{(1+d/a)^2}{\left(\frac{b}{a}\right)E}$ indicates that the sensitivity S is inversely related to modulus E and tip width-to-base ratio $\frac{b}{a}$. One order change of the Young's modulus E boosts one order of the sensitivity. The interstructural separation distance d or distance ratio $\frac{d}{a}$ is proportional to S . A change in the interstructural separation distance by one order can lead to two orders increase in sensitivity. These observations align with earlier conclusions from Sara et al., emphasizing the significance of modulus E and interstructural separation distance d . A detailed investigation into the function $f\left(\frac{d}{a}, k, \frac{b}{a}\right)$ would also elucidate the analysis of the effect of structures and materials on the sensitivity.

Based on the preceding discussion, we can summarize the following points for micro-patterned dielectric CTS:

- The modulus E of dielectrics and the interstructural separation distance d have been identified as two controlling factors that can significantly affect sensitivity in the past research. Notably, a change in the modulus E by an order of magnitude can induce a corresponding order of magnitude change in the initial sensitivity. An increase in the interstructural separation contributes to a higher air volume ratio, resulting in a reduction of the initial capacitance and enhancement of compressibility of dielectrics.
- The geometry of the micropattern dielectrics can fine-tune the sensitivity. In the case of micro-domes, both FEM and experiments indicate that decreasing the dome diameter might be a good way to enhance sensitivity [128]. For micro-pyramids, a smaller tip-width-to-base ratio b/a has been shown to increase sensitivity, primarily by augmenting the compressibility of the dielectrics [39]. For structures such as triangular, circular, and square columns, a heightened sensitivity is observed with an increase in their height. This correlation is attributed to the fact that a greater height results in a more pronounced distance change between two electrodes when compressed, thereby influencing sensitivity [129]. These recommendations highlight the importance of optimizing micro-patterned CTS to improve sensitivity and pressure response, providing valuable guidance for future research and development in this field.

However, it is important to note that there are several limitations in the existing models for micro-patterned dielectric CTS:

- Current models primarily focus on scenarios involving small pressure ranges (<10 kPa), and the sensitivity enhancement strategies from model are only valid for initial sensitivity.

- The trade-off between pressure range and sensitivity was not addressed. Modeling the pressure response of CTS over a wider range of pressures remains unclear.

In addition to micro-patterned dielectric CTS, CTS with foam dielectrics [127] have also gained popularity as common choices for CTS, as depicted in Figure 13.12a. The foam dielectrics are porous polymers with stochastic structures, which are usually fabricated by foaming templates. For example, porous PDMS or Ecoflex can be fabricated by mixing sugar or salt into PDMS or Ecoflex precursor, curing the mixture, and then dissolving sugar or salt. To model the CTS with foam dielectrics using Eq. (13.48) and obtain the sensitivity enhancement strategies based on Eq. (13.50), analytical expressions for the effective dielectric constant and effective Young's modulus of the foam are needed.

The foam can be considered as a two-phase composite of air and polymer, whose effective dielectric constant can be calculated using effective medium theories [130]. For isotropic foam, its effective dielectric constant is found to be within the upper and lower Hashin–Shtrikman bounds [131]:

$$k_p + \frac{3(1-\eta)(k_p-1)}{3+\eta(k_p-1)} < k_{\text{eff}} < k_p - \frac{3k_p\eta(k_p-1)}{3k_p-(1-\eta)(k_p-1)} \quad (13.61)$$

where η is the porosity, k_p is the dielectric constant of the polymer, and k_{eff} is the effective dielectric constant of the porous polymer.

Assuming incompressibility of the polymer, the porosity η under pressure can be estimated as [103]

$$\eta = 1 - \frac{1-\eta_0}{1-\epsilon} \quad (13.62)$$

where η_0 is the initial porosity and ϵ is the compressive strain. Although Hashin–Shtrikman bounds also exist for the modulus of two-phase composites, the modulus–porosity relationships of the polymer foams are more commonly estimated via phenomenological models [132] or analytical models based on certain unit cells [133, 134]. The simplest model for open-cell foams with high porosity is [135, 136]:

$$\frac{E}{E_s} = (1-\eta)^2 \quad (13.63)$$

where E_s is the modulus of the solid polymer.

Note that even though there are mature theoretical studies toward effective Young's modulus (Eq. (13.63)) and effective dielectric constant (Eq. (13.62)) toward foam dielectrics, no one combined these equations in Eqs. (13.48) and (13.50) to get simple analytical equations for CTS with foam dielectrics. Instead, an empirical formula, Eq. (13.64), as illustrated in Figure 13.12b, has been proposed to fit experiment data of sensors' performance:

$$S = \frac{\Delta C_{\text{max}}}{C_0} (1 - e^{-P/P_c}) \quad (13.64)$$

Here, ΔC_{max} represents the saturated capacitance at large pressure, C_0 is the initial capacitance. P is the applied pressure. P_c is the characteristic pressure at which the

capacitance change reaches 63% of its maximum value. In addition, the pressure measurement range (PR) corresponded to 95% of the maximum capacitance change, according to Figure 13.12b, $PR = 3P_c$.

- There is a fair agreement between empirical expression and the experiment with a coefficient of determination R^2 higher than 0.99. However, it is important to highlight that the empirical expression remains somewhat phenomenological, lacking specific guidance for scientists seeking to optimize sensor design.

Nanowire dielectrics are another type of CTS with engineered dielectrics. There are almost no models of nanowire-dielectric CTS. The challenge in modeling nanowire-dielectric CTS stems from its inherent multiscale nature. Addressing this complexity necessitates a homogenization process that transitions nanowire dielectrics from the nano- or microscale to the macroscale. In addition, the intricacy of nanowire dielectrics at the nanoscale is amplified by factors such as geometry, orientation, aspect ratio, distribution, and aggregation of the nanowires, each adding layers of complexity to the homogenization process [75].

13.3.3 Capacitive Tactile Sensors with Engineered Electrodes

CTS with engineered electrodes often incorporate functional fibers or fabric to improve flexibility and conformability for large-area deployment, making them particularly suitable for applications like wearable technology and soft robotics. Qu et al. provided a deeper understanding of textile-based CTS, particularly focusing on their sensitivity [137]. A polymer-based functional fiber was developed using a circular electrode encapsulated by a dielectric layer (Figure 13.13a).

The contact area of the two fibers is assumed to be a double-layer parallel capacitor (Eq. (13.48)), as shown in Figure 13.13b. Due to the relative area of circular electrode change during compression, Eq. (13.50) is revised:

$$S = \frac{d \left(\frac{\Delta C}{C_0} \right)}{\Delta P} = \frac{d_0}{k_0 A_0} \left[\frac{A}{d} \left(\frac{\partial k}{\partial P} \right) + \frac{k}{d} \left(\frac{\partial A}{\partial P} \right) - \frac{k}{A} \left(\frac{\partial d}{\partial P} \right) \right] \quad (13.65)$$

The contact area A_0 that is assumed to be a square with side length a_0 ($A_0 = a_0^2$) becomes A with side length a ($A = a^2$) under compression (Figure 13.13c). Under linear elastic regime, the change in diameter L in compression direction and the thickness of the assumed double-layer parallel capacitor d are described as follows:

$$d = d_0(1 - \epsilon_{\text{compress}}), L = L_0(1 - \epsilon_{\text{compress}}), a = a_0(1 + \epsilon_{\text{lateral}}) \quad (13.66)$$

where $\epsilon_{\text{lateral}}$ and $\epsilon_{\text{compress}}$ is lateral and compressive strain, respectively. Assuming electrodes and dielectric layer have the same Poisson's ratio $\delta = -\epsilon_{\text{lateral}}/\epsilon_{\text{compress}}$,

$$\frac{\partial d}{\partial P} = \frac{d_0 \partial \left(\frac{d}{d_0} \right)}{\partial P} = -\frac{d_0 \partial \epsilon_{\text{compress}}}{\partial P} = -\frac{d_0}{E_{\text{dielectric}}} \quad (13.67)$$

$$\frac{\partial A}{\partial P} = \frac{2a \partial a}{\partial P} = \frac{2a a_0 \partial \left(\frac{a}{a_0} \right)}{\partial P} = \frac{2a a_0 \partial (\epsilon_{\text{lateral}})}{\partial P} = \frac{2a a_0 \nu}{E_{\text{electrode}}} \quad (13.68)$$

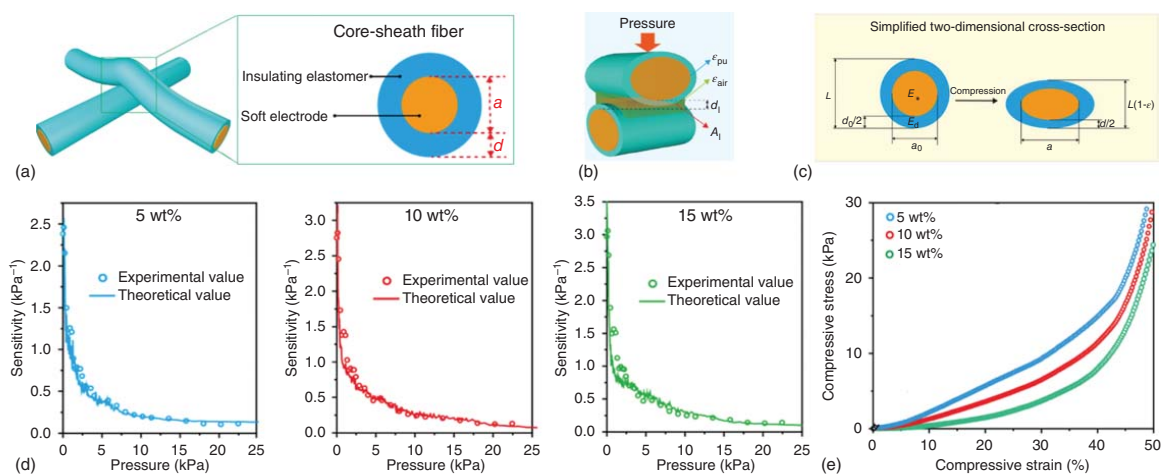


Figure 13.13 CTS with textile electrodes. (a) Schematic of textile CTS. (b) Illustration of the deformation of textile CTS upon compression. (c) Cross-sectional view of the deformation. (d) Comparison of sensitivity versus pressure between experimental and theoretical results for different doping concentrations (5, 10, 15 wt%). (e) Stress-strain curves of the electrodes with different doping concentrations (5, 10, 15 wt%). Source: Reproduced with permission from Ref. [137]. Copyright 2023 American Chemical Society.

Here, $E_{\text{electrode}}$ and $E_{\text{dielectric}}$ stand for Young's modulus of the electrodes and dielectric material, respectively. Hence, the sensitivity can be expressed:

$$S = \frac{d\left(\frac{\Delta C}{C_0}\right)}{dP} = \frac{d_0}{k_0 A_0} \left[\frac{A}{d} \left(\frac{\partial k}{\partial P} \right) + \frac{k}{d} \frac{2aa_0\nu}{E_{\text{electrode}}} + \frac{k}{A} \frac{d_0}{E_{\text{dielectric}}} \right] \quad (13.69)$$

Electrodes doped with CNT in a PU matrix were synthesized through a process involving the mixing of CNT, PU, dimethylformamide (DMF), and water. By altering the doping concentrations to 5, 10, and 15 wt%, electrodes of varying stiffness were obtained, as indicated by different values of $E_{\text{electrode}}$. The theoretical model was found to be consistent with the experimental results, as shown in Figure 13.13d. The experiments yielded following findings: electrodes with a 15 wt% doping concentration displayed the greatest sensitivity, whereas those with a 5 wt% concentration exhibited the least. According to Eq. (13.69), it is deduced that electrodes doped with 15 wt% concentration are expected to be the softest, while those with a 5 wt% doping concentration are anticipated to be the stiffest. This theoretical derivation is in alignment with the experimental results presented in Figure 13.13e.

Based on the sensitivity expression Eq. (13.69), it can be concluded that one strategy to enhance sensitivity is to employ softer electrodes, which is similar to aforementioned strategies.

The exploration of CTS with engineered micro-domes on the electrodes represents another innovative direction in sensor design. As depicted in Figure 13.14a, the electrodes are structured as micro-domes with a rectangular base, while the dielectric materials are flat [138]. This design introduces several key geometric parameters that influence the sensor's performance: h_0 represents the thickness of the dielectric layers, R is the radius of the micro-dome, h_1 is the height of the micro-dome, and h_2 is the height of the rectangle base. The electrical fields passing through the void and dielectric micro-dome are represented by \vec{E}_1 and \vec{E}_2 , respectively. The capacitance of the sensor C is described as $C = C_{01} + C_{02}$. The capacitance is calculated through the expression:

$$C = \frac{-q}{U} \quad (13.70)$$

where q is the total charge quantity and U is the electrical potential. The total electrical quantity q can be determined through the following expression:

$$q = \int \sigma_0 dA \quad (13.71)$$

where σ_0 represents charge density. The charge corresponding to C_{01} and C_{02} is denoted as q_{01} and q_{02} respectively. The charge can be calculated as:

$$q_{01} = \int \sigma_0 dA_1, q_{02} = \int \sigma_0 dA_2 \quad (13.72)$$

where A_1 is the overlapping area between two electrodes and void, A_2 is the surface area of dome respectively. It is assumed that the electrical fields passing through the void \vec{E}_1 and the dielectric materials \vec{E}_2 are uniform. In addition, they posited that the electrical field lines are perpendicular to the dielectric and enter vertically into the dome structures, forming an arc shape, as illustrated in

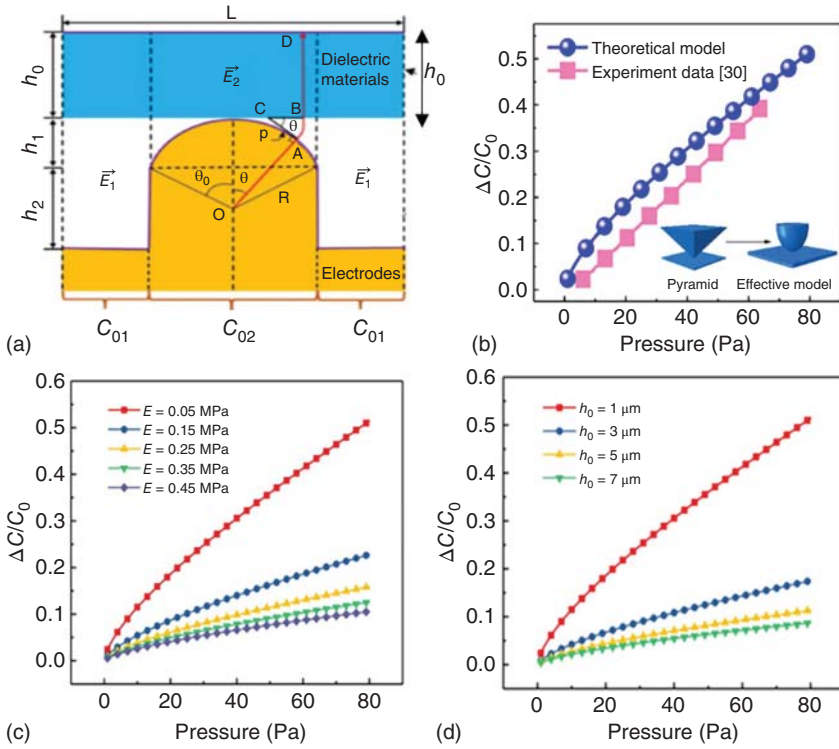


Figure 13.14 CTS with micro-dome electrodes. (a) Schematic of micro-dome electrodes. (b) Theoretical and experimental curves for the relative capacitance change versus pressure. (c) Effects of the Young's modulus of the dielectric material on the relative capacitance change. (d) Effects of the thickness of the dielectric material on the relative capacitance change. Source: Reproduced with permission from Ref. [138]. Copyright 2022 IOP Publishing.

Figure 13.14a. The corresponding electrical potential for C_{01} and C_{02} is U_{01} and U_{02} , respectively.

$$U_{01} = \int_{h_1+h_2} \vec{E}_1 d\vec{l} + \int_{h_0} \vec{E}_2 d\vec{l}, U_{02} = U_{01} \quad (13.73)$$

Hence, the two components of capacitance are described as:

$$C_{01} = \frac{q_{01}}{U_{01}}, C_{02} = \frac{q_{02}}{U_{02}} \quad (13.74)$$

Pressure and sensitivity can be calculated by considering how compression affects the sensor's geometry and electrical properties. When pressure is applied, there is a reduction in h_1 (the height of the micro-dome) and corresponding U_{01} (the electrical potential related to C_{01}). This occurs because the micro-dome electrodes come into contact with the dielectric, altering the electrical field intensity and thus U_{02} (the electrical potential related to C_{02}). Consequently, C_{01} , C_{02} are affected. The relationship between the applied force F and the deflection δ is described by contact mechanics:

$$F = \frac{4}{3}KR^{\frac{1}{2}}\delta^{\frac{3}{2}} \quad (13.75)$$

where R is the radius of micro-domes, K is the contact modulus illustrated in Eq. (13.14). The total contact force is used to calculate the pressure. While sensitivity expression is not explicitly given in the work, the deflection δ was used to update the force and the pressure on the sensors and their corresponding sensitivity.

Due to the absence of direct experimental data for such sensors, the existing data from pyramid electrode-based CTS was adapted to an effective dome shape, thus allowing them to test their theoretical predictions against this modified dataset (Figure 13.14b). Subsequently, they adjusted parameters in the theory to identify the critical parameters affecting sensitivity. In Figure 13.14c, they varied Young's modulus of dielectric materials from 0.05 to 0.45 MPa and plotted relative capacitance changes versus pressure. They found that softer dielectric materials resulted in higher sensitivity. This observation is consistent with previous studies and aligns with the understanding that softer materials allow for greater deformation under pressure, leading to larger changes in capacitance. Additionally, they varied the thickness of the dielectric material from 1 to 7 μm and plotted relative capacitance changes versus pressure. They observed that thinner dielectric materials were associated with higher sensitivity (Figure 13.14d). The authors attributed this phenomenon to the observation for parallel plate capacitors that capacitance changes more rapidly when the distance between the two electrodes is reduced [138].

A common conclusion about softer dielectric materials resulting in higher sensitivity was obtained. The authors assumed the electrical field to be an arc line, which was a good trial to simplify the problem, while a more rigorous study needs to be conducted to validate the assumption. Due to a lack of experimental data for CTS with micro-dome electrodes, they simplified micro-pyramid into an effective micro-dome to validate the theory, which is not that rigorous.

CTS with porous electrodes represents another innovative approach to the design of CTS. These sensors typically consist of a flat dielectric layer sandwiched between a porous elastic electrode and a flat electrode. The unique structure of these sensors makes them particularly sensitive to small pressures.

Zhang et al. fabricated a CTS with an elastic sponge, as shown in Figure 13.15a [139]. The sensor has a sensitivity of 2.25 kPa^{-1} up to 5 kPa (Figure 13.15b). They simplified the porous electrode into a honeycomb structure for the simulation. As illustrated in Figure 13.15c, the electrical field in this configuration does not follow a simple vertical path from the top to the bottom electrode. Instead, it concentrates in areas where the porous electrode makes contact with the dielectric layer. This concentrated electrical field implies that the capacitance change is primarily driven by variations in the contact area between the elastic porous electrode and the dielectric layer. Initially, this contact area is small but increases rapidly under slight pressure and eventually saturates at higher pressures. This behavior explains the ultrahigh sensitivity of these sensors to low pressure.

The COMSOL simulation results (Figure 13.15c) suggest that the contact area between the porous electrode and the dielectric layer is a critical factor in sensor performance. Engineering the contact interface could, therefore, be a key strategy for further enhancing the sensitivity of these sensors. However, the analytical modeling of CTS with porous electrodes presents significant challenges, primarily due to

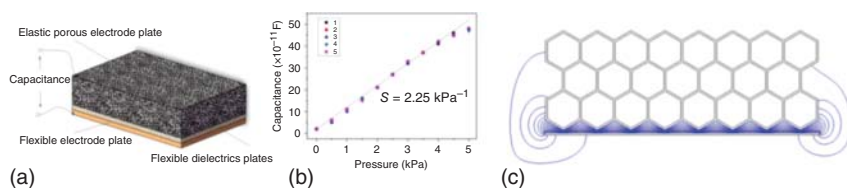


Figure 13.15 CTS with porous electrodes. (a) Schematic of CTS with porous electrodes. (b) Capacitance versus pressure plots of five repetitive tests. (c) COMSOL simulation of the electrical field of CTS with porous electrode. Source: Reproduced with permission from Ref. [139]. Copyright 2018 IOP Publishing.

the non-vertical orientation of the electrical field. Traditional equations that assume a simple, vertical electrical field may not be applicable in this context. This complexity necessitates the development of new theoretical models that can accurately capture the intricate behavior of the electrical field in these porous structures.

13.3.4 Stretchable Capacitive Tactile Sensors

The concept of strain insensitivity initially applied to stretchable RTS can be also extended to stretchable CTS such that we can have a quantitative comparison of the influence of lateral stretch on stretchable CTS.

The mathematical formulation for strain insensitivity in stretchable CTS involves calculating the RMSE and the NRMSE as follows:

$$\text{RMSE} = \sqrt{\frac{\sum_{i=1}^n (C_{P+S}^i - C_P^i)^2}{n}}, \text{NRMSE} = \frac{\text{RMSE}}{\bar{C}_{P+S}}, \text{Strain insensitivity} = 1 - \text{NRMSE} \quad (13.76)$$

Here C_{P+S}^i is the capacitance under both pressure and stretch for the i th observation in the dataset and C_P^i is the capacitance under pressure for the i th observation in the dataset. n is the sample size of the experiment data set. For example, $n = 7$ in Figure 13.16b.

A popular strategy to mitigate the stretch interference is to employ stiff islands to isolate the lateral strain applied to the substrate from the CTS, as exemplified in Figure 13.16a. The CTS comprised three components: the Ecoflex substrate, the

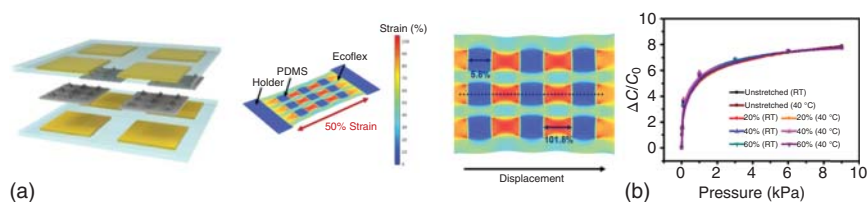


Figure 13.16 Strain isolation through island design. (a) Illustration and strain distribution in the CTS with the stiff island design. (b) The normalized capacitance changes versus pressure under spontaneous stretch and temperature interference. Source: Reproduced with permission from Ref. [140]. Copyright 2019 American Chemical Society.

Table 13.3 Summary of Representative Flexible and Stretchable CTS.

References	Structure	Materials	Mechanism	Sensitivity (kPa ⁻¹) (sensing range [kPa])	Stretch insensitivity (stretchability)
[141]	Film dielectrics	Hydrogel (PAM-LiCl)	High- <i>k</i> dielectrics	~0.0046 (0–27.5)	NM (480%)
[142]	Film dielectrics	SWCNT/PDMS	High- <i>k</i> dielectrics	~0.0059 (0–200)	NM (95%)
[143]	Film dielectrics	VHB Tape	High- <i>k</i> dielectrics	~0.00051 (0–100)	NM (60%)
[29]	Film dielectrics	Ecoflex	High- <i>k</i> dielectrics	~0.0077 (0–20)	NM (10%)
[58]	Nanowire stack	Silicone nanowires	Air gap	~ 1.173 (0–10) ~0.5 (10–50)	NM
[144]	Film dielectrics (Micro-pyramid electrodes)	Graphene/HPU(AgNWs/HPU)	High- <i>k</i> dielectrics/ air gap	~2 (0–3) ~0.6 (3–18)	NM
[145]	Micro-pyramid dielectrics	SiNP/PDMS	Air gap	~1 (0–2) ~0.375 (2–10)	NM
[59]	Porous elastomer dielectrics	CNT elastomer	Air gap	~0.601 (0–10) ~0.4 (10–30) ~0.077 (30–140)	NM
[42]	Film dielectrics (Textile electrode)	Fluorosilicone	Air gap	~0.28 (0–180)	NM
[146]	Wrinkle dielectrics	Ecoflex	Air gap	~0.107 (0–10)	NM
[147]	Film dielectrics	PDMS	Dielectrics	~0.002 (0–500)	NM (5%)
[148]	Film dielectrics	PGS and POMaC	Dielectrics	~0.13 (0–100)	NM (15%)
[149]	Porous dielectrics	Silicone foam	Air gap	~0.0036 (0–250)	0.787 (15%)
[43]	Porous dielectrics w/surface textile	PDMS foam	Air gap	~0.11 (0–25)	NM (30%)
[44]	Porous micro-pyramid	PDMS foam	Air gap	~1.54 (0–1) ~0.601 (1–5) ~0.2 (5–10)	0.98 (60%)
[55]	Film dielectrics	PDMS	Dielectrics	~0.00023 (0–800)	NM (50%)
[150]	Micro-domes	Liquid metal /PDMS	Air gap	~0.17 (0–25)	0.877 (94%) (45%)*

Source: Refs. [38, 42, 43, 70–72, 140–150].

PDMS stiff islands, and the holder. The micro-pyramid-based CTS were located on the PDMS islands, which experienced only a strain of 5.8% when the substrate was stretched by 50%. Figure 13.16b verifies that the curves of normalized capacitance versus pressure nearly coincide, regardless of whether the lateral strain is at 20%, 40%, or 60%.

However, it is important to note that while the island design effectively reduces stretch interference, it can also introduce complexities in design and manufacturing, which might lead to higher production costs and could potentially affect other sensor characteristics, such as sensitivity. As indicated in Table 13.3, CTS employing stretch-mitigation strategies may exhibit lower sensitivity, highlighting a trade-off between sensitivity and stretch insensitivity. Therefore, while strategies like the stiff island design can significantly reduce stretch interference in CTS, they may also bring additional challenges in terms of complexity and sensitivity, which must be carefully considered in the sensor design process.

“PAM-LiCl” denotes poly(acrylamide) – LiCl hydrogel. “SWCNT” denotes single-wall carbon nanotubes. “VHB” is a type of tape in 3M company. “HPU” denotes healable polyurethane. “AgNWs” denotes silver nanowires. “SiNP” denotes silicone nanoparticle. “PGS” denotes poly(glycerol sebacate). “POMaC” denotes poly(octamethylene maleate (anhydride) citrate). “NM” denotes not mentioned. In Ref. [150], the device’s stretchability is stated to be 94%. However, because the graph showing the capacitance versus pressure curve is only provided at a 45% strain, the calculation for strain insensitivity is based on this curve.

13.4 Resistive–Capacitive Hybrid Response Tactile Sensors

13.4.1 Flexible Hybrid Response Tactile Sensors

After decades of development, the performance of RTS and CTS is approaching its limits. However, bottlenecks such as sensitivity–pressure tradeoff and stretch interference persist. The emergence of resistive–capacitive hybrid response tactile sensors (HRTS) has shed some light on possible remedies [151]. The first HRTS was formed by sandwiching a PNC between two parallel electrodes with an ultrathin dielectric layer inserted between the PNC and the electrodes (as illustrated in Figure 13.17a) [151]. The PNC was fabricated from CNT-doped Ecoflex, using commercial nickel foam as a sacrificial template, resulting in an open-cell structure with tubular ligaments and an overall porosity of 86%. The simplified equivalent circuit of HRTS is shown in Figure 13.17b. Due to the resistive nature of the ligaments in the PNC and the parasitic capacitance generated by the air pores, the PNC exhibits a combined response involving both piezoresistivity and piezocapacitance. The ultrathin dielectric layer made of polymethyl methacrylate (PMMA) ensures that the overall sensor remains capacitive. HRTS demonstrates exceptional sensitivity, even under high pressure – a remarkable improvement of up to 423% over conventional CTS within the 10–30 kPa range [151].

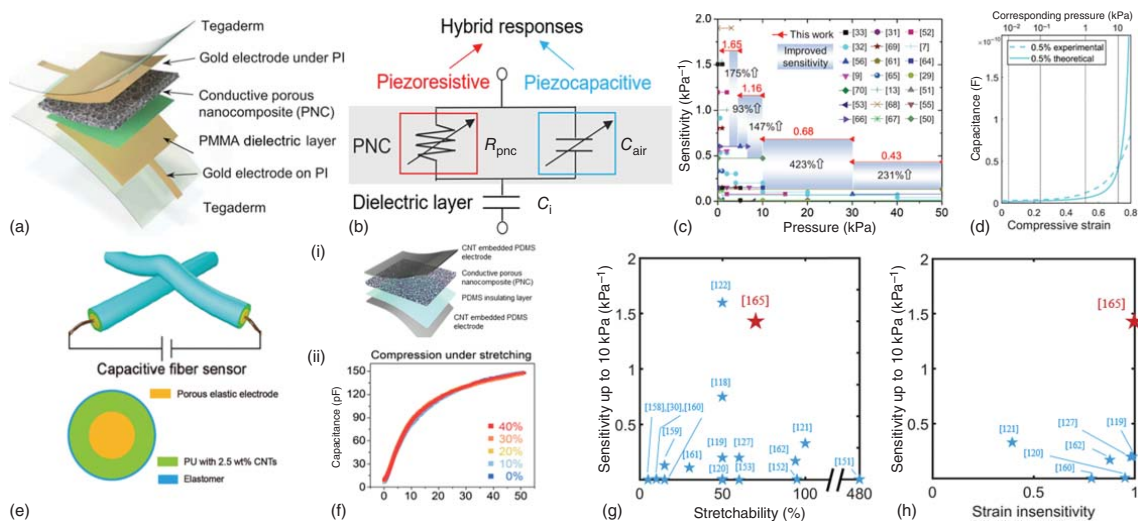


Figure 13.17 HRTS and SHRTS. (a) Schematic of the hybrid response tactile sensors. (b) The equivalent circuit of hybrid response tactile sensor. (c) Comparison of the sensitivity of HRTS with capacitive tactile sensors reported in the literature in the pressure ranges of 1–5, 5–10, 10–30, and 30–50 kPa. (d) The plot of capacitance versus compressive strain for the HRPS with the optimum CNT doping ratio of 0.50 wt%. Source: Reproduced with permission from Ref. [151]. Copyright 2021 John Wiley & Sons. (e) Schematic of the hybrid response fabric CTS. Source: Reproduced with permission from Ref. [152]. Copyright 2023 American Chemical Society. (f) (i) The schematics of stretchable hybrid response tactile sensor. (ii) The capacitance changes versus pressure under spontaneous 0%, 10%, 20%, 30%, and 40% uniaxial stretch [153]. (g) Ashby plot of sensitivity up to 10 kPa⁻¹ of stretchable CTS and stretchable RTS versus stretchability. (h) Ashby plot of sensitivity up to 10 kPa⁻¹ of stretchable CTS and stretchable RTS versus strain insensitivity.

Modeling the electromechanics of HRTS started with modeling the piezoresistive and piezocapacitive behaviors of the PNC. Due to the difficulties of piezoresistive modeling of highly porous and deformable PNC doped at the percolation threshold, the piezoresistive model (R_{PNC} in Figure 13.17b) was just obtained by fitting the experimental measurements of the PNC. The piezocapacitive model (C_{air} in Figure 13.17b) for the PNC assumes the electrical field is uniform and could be simply modeled as a double parallel plate capacitor.

$$C_{\text{air}} = k\epsilon_0 \frac{A}{d} \quad (13.77)$$

where k is the dielectric constant, ϵ_0 is the permittivity of vacuum, A is the relative area of the double parallel plate capacitor, and d is the distance between two electrodes. Plugging the piezoresistive and piezocapacitive models into the simplified circuit given in Figure 13.17b yielded a reasonable prediction of HRTS response up to a pressure of 10 kPa, as shown in Figure 13.17d. This model fails to track the HRTS experiment at large pressure because piezocapacitive model cannot capture the capacitance change when PNC gets more conductive and electrical field is distorted.

Furthering this innovation, Qu et al. reported a fabric HRTS [152], which is composed of an electrode layer (yellow in Figure 13.17e), a porous conductive composite (green in Figure 13.17e), and an insulating layer (blue in Figure 13.17e) [152]. This fabric HRTS has improved the sensitivity by approximately 1081% within the 10–25 kPa range compared to existing fabric CTS [152]. The significant enhancement of sensitivity as demonstrated in the two cases establishes the HRTS as a viable solution to overcoming the sensitivity–pressure trade-off.

13.4.2 Stretchable Hybrid Response Tactile Sensors

The gold electrodes and PMMA dielectric layer in the first HRTS inherently lack stretchability. To create a stretchable hybrid response tactile sensor (SHRTS), the gold electrodes were replaced by CNT spray-coated on PDMS, and the PMMA was replaced by PDMS, as illustrated in Figure 13.17f(i) [153]. These modifications have enabled the SHRTS to achieve a stretchability of up to 70%. When the SHRTS was subjected to combined out-of-plane pressure and in-plane stretching, as depicted in Figure 13.17f(ii) [153], its pressure response curves across varying tensile strains (0–40%) almost overlapped, indicating that the sensor is almost immune from stretch interference. To further highlight the exceptional performance of SHRTS, Figure 13.17g presents an Ashby plot that compares the sensitivity and stretchability of various CTS and RTS, as cataloged in Tables 13.2 and 13.3. In this context, 10 kPa is identified as the pressure relevant to gentle human touch [154]. Marked by a red star on the plot, the SHRTS stands out for its high stretchability, coupled with significant sensitivity, making it highly suitable for nondevelopable and/or inflatable surfaces. Additionally, Figure 13.17h features an Ashby plot of sensitivity versus strain insensitivity for the same range of sensors. Here again, the SHRTS, indicated by the red star, demonstrates its minimal sensitivity to stretching interference while maintaining high sensitivity. These two Ashby plots highlight the

promising future of SHRTS as a stretchable but relatively stretch-insensitive tactile sensor. The electromechanics of SHRTS remain elusive given the large porosity and deformability of the PNC, difficulties in modeling the contact resistance and interface capacitance, as well as the AC effects. We identify these challenges to be a major frontier of the electromechanics of resistive and capacitive pressure sensors with rich opportunities.

13.5 Conclusion and Outlook

13.5.1 Summary of the Existing Achievements

Resistive and capacitive sensors are among the most basic and commonly used modes for tactile sensing in various applications, from robotics to consumer electronics. Over the past two decades, remarkable advancements have been made in engineering these sensors with flexibility and stretchability using soft conductive materials and dielectrics. Many innovative strategies have been employed to bring sensitivity close to that of human skin (around 2 kPa^{-1}) at small pressures (i.e. 10 kPa) [155, 156]. These strategies include engineering the contact and tunneling resistance in RTS [29, 157], utilizing high- k materials, and/or incorporating air gaps in CTS [157, 158]. In limited cases, exceptional sensitivity (4.7 kPa^{-1}) has been achieved in high-pressure regimes ($10\text{--}100 \text{ kPa}$) [111]. This chapter outlines existing electromechanical models to facilitate the understanding and future development of RTS and CTS, which are briefly summarized as follows:

- Resistive Tactile Sensors (RTS):** We have categorized the pressure-sensing components in RTS into three major mechanisms – microstructured contacts, bulk conductive nanocomposites, and porous conductive materials. In the first case, if contact resistance is dominating, decreasing Young's modulus of sensing materials increases the sensitivity. Compared with regular structures like micro-pyramids and micro-domes, RDS may have more contact area change. For bulk conductive nanocomposite-based RTS, the concentration of the filler and the modulus of the composite are two essential parameters for the sensor design. Porous conductive materials are basically a combination of the first two mechanisms, which could lead to an enhancement of the sensitivity and sensing range beyond the individual ones.
- Capacitive Tactile Sensors (CTS):** We have divided CTS into engineered dielectrics and engineered electrodes. For CTS with engineered dielectrics, it is well recognized that the Young's modulus and the volume fraction of air of the dielectric layer are critical design parameters. A decrease in modulus or an increase in air volume fraction can enhance sensitivity but may compromise the sensing range. In comparison, structural characteristics might be less influential on these sensors. For CTS with engineered electrodes, the Young's moduli of both the dielectric and the electrodes matter. Since the electric field in those CTS

differs from those of parallel plate capacitors, identifying crucial parameters can be challenging.

- **Hybrid Response Tactile Sensors (HRTS):** By merging resistive and capacitive responses in one sensor, HRTS, as described in Section 13.4, has demonstrated the potential to overcome some major bottlenecks of RTS and CTS, such as sensitivity-pressure tradeoff and stretch interference [68, 151]. However, HRTS are still in their infancy, and the electromechanical understandings are still very limited. A major difference between HRTS and conventional resistive and CTS lies in their AC frequency-dependent behaviors [159], which opens a new avenue of device tuning and readout circuit engineering.

13.5.2 Remaining Challenges and Future Prospects

While extensive research efforts have been invested in constructing and enhancing the materials and structures used in RTS and CTS, important device details are often insufficiently documented. These include parameters such as electrode and sensing material sizes, initial resistance or capacitance before deformation, electrode contact (separate or integrated with the sensing material), and specifics of the test apparatus. Likewise, inconsistencies in reporting and comparing sensor performance data, including the use of $\Delta I/I_0$ or $\Delta R/R_0$ to present RTS results, and sensitivity evaluated at different pressure magnitudes or ranges, need to be addressed. By harmonizing experimental setups and data reporting, it could pave the way to greater use of machine learning and artificial intelligence for sensor design, sparking innovation in resistive and capacitive tactile sensors.

Additionally, while methods of modeling and simulation to explore the electromechanics of these sensors are commonly used, the details of these methods often lack clarity. There have been only a limited number of comprehensive attempts to elucidate the relationship between factors like Young's modulus, sensor structures, and sensor performance. Some models, like those based on tunneling effects, can be too intricate for immediate use by sensor developers, while others, such as those involving porous materials with stochastic structures, are difficult to simplify and quantify. For example, even in instances of simple structures like micro-domes and micro-pyramids, existing models typically apply to specific cases rather than providing a broader set of guidelines for future research.

To advance the field, it is urgently required to develop a foundational and universally applicable theoretical and numerical modeling framework. This should be grounded in physics, yet feasibly be adopted by engineers. One of the main challenges lies in creating simplified electromechanical models that encapsulate the primary mechanisms and control parameters of resistive and capacitive tactile sensors. This is inherently complex due to the intricate interplay between material properties, sensor structures, and multi-directional mechanical stress. However, simplifications informed by experiments and multiscale modeling in mechanics can be expanded to the research on the electromechanics of RTS and CTS.

Acknowledgments

NL acknowledges the U.S. National Science Foundation (NSF) Grant ASCENT-2133106, the U.S. Army Research Office (ARO) under Cooperative Agreement W911NF-19-2-0333, and the U.S. Office of Naval Research (ONR) Grant N00014-20-1-2112, the U.S. Defense Health Agency (DRA) STTR Grant HT942523C0039. ZZ acknowledges the National Aeronautics and Space Administration (NASA) of the United States under Cooperative Agreement 80NSSC18M0022.

References

- 1 Johnson, K.O. (2001). The roles and functions of cutaneous mechanoreceptors. *Current Opinion in Neurobiology* 11 (4): 455–461.
- 2 Chortos, A., Liu, J., and Bao, Z.A. (2016). Pursuing prosthetic electronic skin. *Nature Materials* 15 (9): 937–950.
- 3 Dargahi, J. and Najarian, S. (2004). Human tactile perception as a standard for artificial tactile sensing—a review. *The International Journal of Medical Robotics and Computer Assisted Surgery* 1 (1): 23–35.
- 4 McLellan, K., Petrofsky, J.S., Zimmerman, G. et al. (2009). The influence of environmental temperature on the response of the skin to local pressure: the impact of aging and diabetes. *Diabetes Technology & Therapeutics* 11 (12): 791–798.
- 5 Tepole, A.B., Gosain, A.K., and Kuhl, E. (2012). Stretching skin: the physiological limit and beyond. *International Journal of Non-Linear Mechanics* 47 (8): 938–949.
- 6 Yu, B., Kang, S.Y., Akthakul, A. et al. (2016). An elastic second skin. *Nature Materials* 15 (8): 911–918.
- 7 Wang, X., Dong, L., Zhang, H. et al. (2015). Recent progress in electronic skin. *Advanced Science* 2 (10): 1500169.
- 8 Lee, W.W., Tan, Y.J., Yao, H. et al. (2019). A neuro-inspired artificial peripheral nervous system for scalable electronic skins. *Science Robotics* 4 (32): eaax2198.
- 9 Wang, M., Luo, Y., Wang, T. et al. (2021). Artificial skin perception. *Advanced Materials* 33 (19): 2003014.
- 10 Kim, Y., Chortos, A., Xu, W. et al. (2018). A bioinspired flexible organic artificial afferent nerve. *Science* 360 (6392): 998–1003.
- 11 Park, J., Kim, M., Lee, Y. et al. (2015). Fingertip skin-inspired microstructured ferroelectric skins discriminate static/dynamic pressure and temperature stimuli. *Science Advances* 1 (9): e1500661.
- 12 Chen, J., Zhang, J., Hu, J. et al. (2022). Ultrafast-response/recovery flexible piezoresistive sensors with DNA-like double helix yarns for epidermal pulse monitoring. *Advanced Materials* 34 (2): e2104313.
- 13 Gu, G., Zhang, N., Xu, H. et al. (2023). A soft neuroprosthetic hand providing simultaneous myoelectric control and tactile feedback. *Nature Biomedical Engineering* 7 (4): 589–598.

- 14 Zhou, K., Zhao, Y., Sun, X. et al. (2020). Ultra-stretchable triboelectric nanogenerator as high-sensitive and self-powered electronic skins for energy harvesting and tactile sensing. *Nano Energy* 70: 104546.
- 15 Lee, B., Oh, J.Y., Cho, H. et al. (2020). Ultraflexible and transparent electroluminescent skin for real-time and super-resolution imaging of pressure distribution. *Nature Communications* 11 (1): 663.
- 16 Su, Z., Fishel, J.A., Yamamoto, T., and Loeb, G.E. (2012). Use of tactile feedback to control exploratory movements to characterize object compliance. *Frontiers in Neurorobotics* 6: 7.
- 17 Kaboli, M., Yao, K., Feng, D., and Cheng, G. (2018). Tactile-based active object discrimination and target object search in an unknown workspace. *Autonomous Robots* 43 (1): 123–152.
- 18 Huang, X., Guo, W., Liu, S. et al. (2022). Flexible mechanical metamaterials enabled electronic skin for real-time detection of unstable grasping in robotic manipulation. *Advanced Functional Materials* 32 (23): 2109109.
- 19 Bergner, F., Dean-Leon, E., and Cheng, G. (2020). Design and realization of an efficient large-area event-driven e-skin. *Sensors* 20 (7): 1965.
- 20 Park, D.Y., Joe, D.J., Kim, D.H. et al. (2017). Self-powered real-time arterial pulse monitoring using ultrathin epidermal piezoelectric sensors. *Advanced Materials* 29 (37): 1702308.
- 21 Lou, Z., Chen, S., Wang, L. et al. (2017). Ultrasensitive and ultraflexible e-skins with dual functionalities for wearable electronics. *Nano Energy* 38: 28–35.
- 22 Dahiya, R., Yogeswaran, N., Liu, F. et al. (2019). Large-area soft e-skin: the challenges beyond sensor designs. *Proceedings of the IEEE* 107 (10): 2016–2033.
- 23 Yin, R., Wang, D., Zhao, S. et al. (2020). Wearable sensors-enabled human-machine interaction systems: from design to application. *Advanced Functional Materials* 31 (11): 2008936.
- 24 Kang, H., Zhao, C., Huang, J. et al. (2019). Fingerprint-inspired conducting hierarchical wrinkles for energy-harvesting e-skin. *Advanced Functional Materials* 29 (43): 1903580.
- 25 Byun, J., Lee, Y., Yoon, J. et al. (2018). Electronic skins for soft, compact, reversible assembly of wirelessly activated fully soft robots. *Science Robotics* 3 (18): eaas9020.
- 26 Bao, L., Han, C., Li, G. et al. (2023). Flexible electronic skin for monitoring of grasping state during robotic manipulation. *Soft Robotics* 10 (2): 336–344.
- 27 Zhang, C., Liu, S., Huang, X. et al. (2019). A stretchable dual-mode sensor array for multifunctional robotic electronic skin. *Nano Energy* 62: 164–170.
- 28 Pyo, S., Lee, J., Bae, K. et al. (2021). Recent progress in flexible tactile sensors for human-interactive systems: from sensors to advanced applications. *Advanced Materials* 33 (47): 2005902.
- 29 Pierre Claver, U. and Zhao, G. (2021). Recent progress in flexible pressure sensors based electronic skin. *Advanced Engineering Materials* 23 (5): 2001187.
- 30 Liu, Y., Bao, R., Tao, J. et al. (2020). Recent progress in tactile sensors and their applications in intelligent systems. *Science Bulletin* 65 (1): 70–88.

- 31 Dahiya, R.S., Mittendorfer, P., Valle, M. et al. (2013). Directions toward effective utilization of tactile skin: a review. *IEEE Sensors Journal* 13 (11): 4121–4138.
- 32 Wan, Y., Wang, Y., and Guo, C.F. (2017). Recent progresses on flexible tactile sensors. *Materials Today Physics* 1: 61–73.
- 33 He, K., Hou, Y., Yi, C. et al. (2020). High-performance zero-standby-power-consumption-under-bending pressure sensors for artificial reflex arc. *Nano Energy* 73, 104743.
- 34 Li, Z., Qiang, F., Dai, S.W. et al. (2019). Construction of sandwich-like porous structure of graphene-coated foam composites for ultrasensitive and flexible pressure sensor. *Nanoscale* 11: 10229–10238.
- 35 Lee, Y., Park, J., Cho, S. et al. (2018). Flexible ferroelectric sensors with ultra-high pressure sensitivity and linear response over exceptionally broad pressure range. *ACS Nano* 12 (4): 4045–4054.
- 36 Liu, M., Pu, X., Jiang, C. et al. (2017). Large-area all-textile pressure sensors for monitoring human motion and physiological signals. *Advanced Materials* 29 (41): 1703700.
- 37 Lee, S., Reuveny, A., Reeder, J. et al. (2016). A transparent bending-insensitive pressure sensor. *Nature Nanotechnology* 11 (5): 472–478.
- 38 Shi, H., Al-Rubaiai, M., Holbrook, C.M. et al. (2019). Screen-printed soft capacitive sensors for spatial mapping of both positive and negative pressures. *Advanced Functional Materials* 29 (23): 1809116.
- 39 Ruth, S.R.A., Beker, L., Tran, H. et al. (2019). Rational design of capacitive pressure sensors based on pyramidal microstructures for specialized monitoring of biosignals. *Advanced Functional Materials* 30: 1903100.
- 40 Wan, Y., Qiu, Z., Huang, J. et al. (2018). Natural plant materials as dielectric layer for highly sensitive flexible electronic skin. *Small* 14 (35): e1801657.
- 41 Núñez, C.G., Navaraj, W.T., Polat, E.O. et al. (2017). Energy-autonomous, flexible, and transparent tactile skin. *Advanced Functional Materials* 27 (18): 1606287.
- 42 Viry, L., Levi, A., Totaro, M. et al. (2014). Flexible three-axial force sensor for soft and highly sensitive artificial touch. *Advanced Materials* 26 (17): 2659–2664.
- 43 Park, S., Kim, H., Vosgueritchian, M. et al. (2014). Stretchable energy-harvesting tactile electronic skin capable of differentiating multiple mechanical stimuli modes. *Advanced Materials* 26 (43): 7324–7332.
- 44 Mannsfeld, S.C., Tee, B.C., Stoltenberg, R.M. et al. (2010). Highly sensitive flexible pressure sensors with microstructured rubber dielectric layers. *Nature Materials* 9 (10): 859–864.
- 45 Li, R.Y., Si, Y., Zhu, Z. et al. (2017). Supercapacitive iontronic nanofabric sensing. *Advanced Materials* 29 (36): 1700253.
- 46 Chorsi, M.T., Curry, E.J., Chorsi, H.T. et al. (2019). Piezoelectric biomaterials for sensors and actuators. *Advanced Materials* 31 (1): 1802084.

- 47 Chun, J., Lee, K.Y., Kang, C.Y. et al. (2014). Embossed hollow hemisphere-based piezoelectric nanogenerator and highly responsive pressure sensor. *Advanced Functional Materials* 24 (14): 2038–2043.
- 48 Choi, W., Lee, J., Kyoung Yoo, Y. et al. (2014). Enhanced sensitivity of piezoelectric pressure sensor with microstructured polydimethylsiloxane layer. *Applied Physics Letters* 104 (12): 123701.
- 49 Garcia, C., Trendafilova, I., de Villoria, R.G., and del Rio, J.S. (2018). Self-powered pressure sensor based on the triboelectric effect and its analysis using dynamic mechanical analysis. *Nano Energy* 50: 401–409.
- 50 Ramuz, M., Tee, B.C., Tok, J.B., and Bao, Z. (2012). Transparent, optical, pressure-sensitive artificial skin for large-area stretchable electronics. *Advanced Materials* 24 (24): 3223–3227.
- 51 Yamada, Y., Morizono, T., Umetani, Y., and Takahashi, H. (2005). Highly soft viscoelastic robot skin with a contact object-location-sensing capability. *IEEE Transactions on Industrial Electronics* 52 (4): 960–968.
- 52 Zhou, Y., Zhao, X., Xu, J. et al. (2021). Giant magnetoelastic effect in soft systems for bioelectronics. *Nature Materials* 20 (12): 1670–1676.
- 53 Yang, T.T., Xie, D., Li, Z., and Zhu, H. (2017). Recent advances in wearable tactile sensors: materials, sensing mechanisms, and device performance. *Materials Science & Engineering R: Reports* 115: 1–37.
- 54 Chang, Y., Wang, L., Li, R. et al. (2021). First decade of interfacial iontronic sensing: from droplet sensors to artificial skins. *Advanced Materials* 33 (7): e2003464.
- 55 Xiong, Y., Han, J., Wang, Y. et al. (2022). Emerging iontronic sensing: materials, mechanisms, and applications. *Research* 2022: 9867378.
- 56 Sezer, N. and Koç, M. (2021). A comprehensive review on the state-of-the-art of piezoelectric energy harvesting. *Nano Energy* 80: 105567.
- 57 Meng, K., Xiao, X., Wei, W. et al. (2022). Wearable pressure sensors for pulse wave monitoring. *Advanced Materials* 34 (21): e2109357.
- 58 Wang, B. and Facchetti, A. (2019). Mechanically flexible conductors for stretchable and wearable e-skin and e-textile devices. *Advanced Materials* 31 (28): e1901408.
- 59 Rus, D. and Tolley, M.T. (2015). Design, fabrication and control of soft robots. *Nature* 521 (7553): 467–475.
- 60 Shepherd, R.F., Ilievski, F., Choi, W. et al. (2011). Multigait soft robot. *Proceedings of the National Academy of Sciences of the United States of America* 108 (51): 20400–20403.
- 61 Rich, S.I., Wood, R.J., and Majidi, C. (2018). Untethered soft robotics. *Nature Electronics* 1 (2): 102–112.
- 62 Sachyani Keneth, E., Kamyshny, A., Totaro, M. et al. (2021). 3D printing materials for soft robotics. *Advanced Materials* 33 (19): e2003387.
- 63 Duan, Y., He, S., Wu, J. et al. (2022). Recent progress in flexible pressure sensor arrays. *Nanomaterials* 12 (14): 2495.

- 64 He, J., Zhang, Y., Zhou, R. et al. (2020). Recent advances of wearable and flexible piezoresistivity pressure sensor devices and its future prospects. *Journal of Materiomics* 6 (1): 86–101.
- 65 Nie, Z., Kwak, J.W., Han, M., and Rogers, J.A. (2022). Mechanically active materials and devices for bio-interfaced pressure sensors—a review. *Advanced Materials* e2205609.
- 66 Li, J., Bao, R., Tao, J. et al. (2018). Recent progress in flexible pressure sensor arrays: from design to applications. *Journal of Materials Chemistry C* 6 (44): 11878–11892.
- 67 Li, R., Zhou, Q., Bi, Y. et al. (2021). Research progress of flexible capacitive pressure sensor for sensitivity enhancement approaches. *Sensors and Actuators A: Physical* 321: 112425.
- 68 Ha, K.-H., Huh, H., Li, Z., and Lu, N. (2022). Soft capacitive pressure sensors: trends, challenges, and perspectives. *ACS Nano* 16 (3): 3442–3448.
- 69 Li, S., Zhang, Y., Wang, Y. et al. (2019). Physical sensors for skin-inspired electronics. *InfoMat* 2 (1): 184–211.
- 70 Lipomi, D.J., Vosgueritchian, M., Tee, B.C. et al. (2011). Skin-like pressure and strain sensors based on transparent elastic films of carbon nanotubes. *Nature Nanotechnology* 6 (12): 788–792.
- 71 Cheng, W., Yu, L., Kong, D. et al. (2018). Fast-response and low-hysteresis flexible pressure sensor based on silicon nanowires. *IEEE Electron Device Letters* 39 (7): 1069–1072.
- 72 Kwon, D., Lee, T.I., Kim, M.S., et al. (2015). Porous dielectric elastomer based ultra-sensitive capacitive pressure sensor and its application to wearable sensing device. In *2015 Transducers-2015 18th International Conference on Solid-State Sensors, Actuators and Microsystems (TRANSDUCERS)*. IEEE. pp. 299–302.
- 73 Li, L., Fu, X., Chen, S. et al. (2020). Hydrophobic and stable MXene-polymer pressure sensors for wearable electronics. *ACS Applied Materials & Interfaces* 12 (13): 15362–15369.
- 74 Choong, C.L., Shim, M.B., Lee, B.S. et al. (2014). Highly stretchable resistive pressure sensors using a conductive elastomeric composite on a micropylramid array. *Advanced Materials* 26 (21): 3451–3458.
- 75 Li, J., Fang, L., Sun, B. et al. (2020). Review—recent progress in flexible and stretchable piezoresistive sensors and their applications. *Journal of the Electrochemical Society* 167 (3): 037561.
- 76 Mishra, R.B., El-Atab, N., Hussain, A.M., and Hussain, M.M. (2021). Recent progress on flexible capacitive pressure sensors: from design and materials to applications. *Advanced Materials Technologies* 6 (4): 2001023.
- 77 Ma, C., Xu, D., Huang, Y.C. et al. (2020). Robust flexible pressure sensors made from conductive micropylramids for manipulation tasks. *ACS Nano* 14 (10): 12866–12876.
- 78 Doshi, S.M. and Thostenson, E.T. (2018). Thin and flexible carbon nanotube-based pressure sensors with ultrawide sensing range. *ACS Sensors* 3 (7): 1276–1282.

- 79 Jason, N.N., Ho, M.D., and Cheng, W. (2017). Resistive electronic skin. *Journal of Materials Chemistry C* 5 (24): 5845–5866.
- 80 Dai, H. and Thostenson, E.T. (2019). Large-area carbon nanotube-based flexible composites for ultra-wide range pressure sensing and spatial pressure mapping. *ACS Applied Materials & Interfaces* 11 (51): 48370–48380.
- 81 Zhang, L., Li, H., Lai, X. et al. (2018). Thiolated graphene@polyester fabric-based multilayer piezoresistive pressure sensors for detecting human motion. *ACS Applied Materials & Interfaces* 10 (48): 41784–41792.
- 82 Mao, Y., Ji, B., Chen, G. et al. (2019). Robust and wearable pressure sensor assembled from AgNW-coated PDMS micropillar sheets with high sensitivity and wide detection range. *ACS Applied Nano Materials* 2 (5): 3196–3205.
- 83 Liu, S., Wu, X., Zhang, D. et al. (2017). Ultrafast dynamic pressure sensors based on graphene hybrid structure. *ACS Applied Materials & Interfaces* 9 (28): 24148–24154.
- 84 Dintwa, E., Tijsskens, E., and Ramon, H. (2008). On the accuracy of the Hertz model to describe the normal contact of soft elastic spheres. *Granular Matter* 10: 209–221.
- 85 Persson, B. (2022). On the electric contact resistance. *Tribology Letters* 70 (3): 88.
- 86 Ji, B., Zhou, Q., Wu, J. et al. (2020). Synergistic optimization toward the sensitivity and linearity of flexible pressure sensor via double conductive layer and porous microdome array. *ACS Applied Materials & Interfaces* 12 (27): 31021–31035.
- 87 Ruschau, G., Yoshikawa, S., and Newnham, R. (1992). Resistivities of conductive composites. *Journal of Applied Physics* 72 (3): 953–959.
- 88 Khalili, N., Naguib, H., and Kwon, R. (2016). A constriction resistance model of conjugated polymer based piezoresistive sensors for electronic skin applications. *Soft Matter* 12 (18): 4180–4189.
- 89 Park, J., Lee, Y., Hong, J. et al. (2014). Giant tunneling piezoresistance of composite elastomers with interlocked microdome arrays for ultrasensitive and multimodal electronic skins. *ACS Nano* 8 (5): 4689–4697.
- 90 Greenwood, J.A. (1966). Constriction resistance and the real area of contact. *British Journal of Applied Physics* 17 (12): 1621.
- 91 Zhu, B., Niu, Z., Wang, H. et al. (2014). Microstructured graphene arrays for highly sensitive flexible tactile sensors. *Small* 10 (18): 3625–3631.
- 92 Park, H., Jeong, Y.R., Yun, J. et al. (2015). Stretchable array of highly sensitive pressure sensors consisting of polyaniline nanofibers and Au-coated polydimethylsiloxane micropillars. *ACS Nano* 9 (10): 9974–9985.
- 93 Bae, G.Y., Pak, S.W., Kim, D. et al. (2016). Linearly and highly pressure-sensitive electronic skin based on a bioinspired hierarchical structural array. *Advanced Materials* 28 (26): 5300–5306.
- 94 Pang, Y., Zhang, K., Yang, Z. et al. (2018). Epidermis microstructure inspired graphene pressure sensor with random distributed spinosum for high sensitivity and large linearity. *ACS Nano* 12 (3): 2346–2354.

- 95 Kanoun, O., Bouhamed, A., Ramalingame, R. et al. (2021). Review on conductive polymer/CNTs nanocomposites based flexible and stretchable strain and pressure sensors. *Sensors* 21 (2): 341.
- 96 Ding, S., Han, B., Dong, X. et al. (2017). Pressure-sensitive behaviors, mechanisms and model of field assisted quantum tunneling composites. *Polymer* 113: 105–118.
- 97 Roldughin, V. and Vysotskii, V. (2000). Percolation properties of metal-filled polymer films, structure and mechanisms of conductivity. *Progress in Organic Coatings* 39 (2–4): 81–100.
- 98 Luheng, W., Tianhuai, D., and Peng, W. (2009). Influence of carbon black concentration on piezoresistivity for carbon-black-filled silicone rubber composite. *Carbon* 47 (14): 3151–3157.
- 99 Luheng, W., Tianhuai, D., and Peng, W. (2007). Effects of conductive phase content on critical pressure of carbon black filled silicone rubber composite. *Sensors and Actuators A: Physical* 135 (2): 587–592.
- 100 Hou, Y., Wang, D., Zhang, X.M. et al. (2013). Positive piezoresistive behavior of electrically conductive alkyl-functionalized graphene/polydimethylsilicone nanocomposites. *Journal of Materials Chemistry C* 1 (3): 515–521.
- 101 Zhang, X.W., Pan, Y., Zheng, Q., and Yi, X.S. (2000). Time dependence of piezoresistance for the conductor-filled polymer composites. *Journal of Polymer Science Part B: Polymer Physics* 38 (21): 2739–2749.
- 102 Kirpluks, M., Cabulis, U., Andersons, J. et al. (2018). Modeling the effect of foam density and strain rate on the compressive response of polyurethane foams. *SAE International Journal of Materials and Manufacturing* 11 (2): 131–138.
- 103 Zhang, J., Wang, Z., and Peng, Z. (2021). Analytical model of the piezoresistive behavior of highly compressible sensors made of microporous nanocomposites. *Advanced Theory and Simulations* 4 (12): 2100247.
- 104 Li, W., Jin, X., Han, X. et al. (2021). Synergy of porous structure and microstructure in piezoresistive material for high-performance and flexible pressure sensors. *ACS Applied Materials & Interfaces* 13 (16): 19211–19220.
- 105 Xu, J., Li, H., Yin, Y. et al. (2022). High sensitivity and broad linearity range pressure sensor based on hierarchical in-situ filling porous structure. *npj Flexible Electronics* 6 (1): 62.
- 106 Storåkers, B. (1986). On material representation and constitutive branching in finite compressible elasticity. *Journal of the Mechanics and Physics of Solids* 34 (2): 125–145.
- 107 Balberg, I. (1986). Excluded-volume explanation of Archie's law. *Physical Review B* 33 (5): 3618.
- 108 Chen, R., Luo, T., Wang, J. et al. (2023). Nonlinearity synergy: an elegant strategy for realizing high-sensitivity and wide-linear-range pressure sensing. *Nature Communications* 14 (1): 6641.
- 109 Bang, J., Chun, B., Lim, J. et al. (2023). Ultra-broad linear range and sensitive flexible piezoresistive sensor using reversed lattice structure for wearable electronics. *ACS Applied Materials & Interfaces* 15 (28): 34120–34131.

- 110 Chen, J., Chen, K., Jin, J. et al. (2023). Outstanding synergy of sensitivity and linear range enabled by multigradient architectures. *Nano Letters* 23: 11958–11967.
- 111 Zhang, Y., Lu, Q., He, J. et al. (2023). Localizing strain via micro-cage structure for stretchable pressure sensor arrays with ultralow spatial crosstalk. *Nature Communications* 14 (1): 1252.
- 112 Ding, X., Zhong, W., Jiang, H. et al. (2020). Highly accurate wearable piezoresistive sensors without tension disturbance based on weaved conductive yarn. *ACS Applied Materials & Interfaces* 12 (31): 35638–35646.
- 113 Chou, H.-H., Nguyen, A., Chortos, A. et al. (2015). A chameleon-inspired stretchable electronic skin with interactive colour changing controlled by tactile sensing. *Nature Communications* 6 (1): 8011.
- 114 Su, Q., Zou, Q., Li, Y. et al. (2021). A stretchable and strain-unperturbed pressure sensor for motion interference—free tactile monitoring on skins. *Science Advances* 7 (48): eabi4563.
- 115 Matsuda, R., Mizuguchi, S., Nakamura, F. et al. (2020). Highly stretchable sensing array for independent detection of pressure and strain exploiting structural and resistive control. *Scientific Reports* 10 (1): 12666.
- 116 Lee, G., Son, J., Kim, D. et al. (2022). Crocodile-skin-inspired omnidirectionally stretchable pressure sensor. *Small* 18 (52): e2205643.
- 117 Xu, T., Ding, Y., Wang, Z. et al. (2017). Three-dimensional and ultralight sponges with tunable conductivity assembled from electrospun nanofibers for a highly sensitive tactile pressure sensor. *Journal of Materials Chemistry C* 5 (39): 10288–10294.
- 118 Li, X., Li, X., Liu, T. et al. (2021). Wearable, washable, and highly sensitive piezoresistive pressure sensor based on a 3D sponge network for real-time monitoring human body activities. *ACS Applied Materials & Interfaces* 13 (39): 46848–46857.
- 119 Yue, Y., Liu, N., Liu, W. et al. (2018). 3D hybrid porous Mxene-sponge network and its application in piezoresistive sensor. *Nano Energy* 50: 79–87.
- 120 Yang, J., Tang, D., Ao, J. et al. (2020). Ultrasoft liquid metal elastomer foams with positive and negative piezopermittivity for tactile sensing. *Advanced Functional Materials* 30 (36): 2002611.
- 121 Ruth, S.R.A. and Bao, Z. (2020). Designing tunable capacitive pressure sensors based on material properties and microstructure geometry. *ACS Applied Materials & Interfaces* 12 (52): 58301–58316.
- 122 Javidi, R., Moghimi Zand, M., and Alizadeh Majd, S. (2023). Designing wearable capacitive pressure sensors with arrangement of porous pyramidal microstructures. *Micro and Nano Systems Letters* 11 (1): 13.
- 123 Tee, B.C.K., Chortos, A., Dunn, R.R. et al. (2014). Tunable flexible pressure sensors using microstructured elastomer geometries for intuitive electronics. *Advanced Functional Materials* 24 (34): 5427–5434.
- 124 Boutry, C.M., Negre, M., Jorda, M. et al. (2018). A hierarchically patterned, bioinspired e-skin able to detect the direction of applied pressure for robotics. *Science Robotics* 3 (24): eaau6914.

- 125 Luo, Y.S., Shao, J., Chen, S. et al. (2019). Flexible capacitive pressure sensor enhanced by tilted micropillar arrays. *ACS Applied Materials & Interfaces* 11 (19): 17796–17803.
- 126 Peng, S.H., Blanloeuil, P., Wu, S., and Wang, C.H. (2018). Rational design of ultrasensitive pressure sensors by tailoring microscopic features. *Advanced Materials Interfaces* 5 (18): 1800403.
- 127 Bilent, S., Dinh, T.H.N., Martincic, E., and Joubert, P.Y. (2019). Influence of the porosity of polymer foams on the performances of capacitive flexible pressure sensors. *Sensors* 19 (9): 1968.
- 128 Zhang, Y., Hu, Y., Zhu, P. et al. (2017). Flexible and highly sensitive pressure sensor based on microdome-patterned PDMS forming with assistance of colloid self-assembly and replica technique for wearable electronics. *ACS Applied Materials & Interfaces* 9 (41): 35968–35976.
- 129 Zhang, W., Sun, W., Xiao, W. et al. (2019). Numerical simulation analysis of microstructure of dielectric layers in capacitive pressure sensors. *IEEE Sensors Journal* 19 (9): 3260–3266.
- 130 Choy, T.C. (2015). *Effective Medium Theory: Principles and Applications*, vol. 165. Oxford University Press.
- 131 Hashin, Z. and Shtrikman, S. (1962). A variational approach to the theory of the effective magnetic permeability of multiphase materials. *Journal of Applied Physics* 33 (10): 3125–3131.
- 132 Progelhof, R. and Throne, J.L. (1979). Young's modulus of uniform density thermoplastic foam. *Polymer Engineering & Science* 19 (7): 493–499.
- 133 Gong, L., Kyriakides, S., and Jang, W.Y. (2005). Compressive response of open-cell foams. Part I: morphology and elastic properties. *International Journal of Solids and Structures* 42 (5–6): 1355–1379.
- 134 Choi, J. and Lakes, R.S. (1995, 1995). Analysis of elastic modulus of conventional foams and of re-entrant foam materials with a negative Poisson's ratio. *International Journal of Mechanical Sciences* 37 (1): 51–59.
- 135 Moore, D., Couzens, K., and Iremonger, M.J. (1974). The deformational behaviour of foamed thermoplastics. *Journal of Cellular Plastics* 10 (3): 135–139.
- 136 Gibson, I.J. and Ashby, M.F. (1982). The mechanics of three-dimensional cellular materials. *Proceedings of the Royal Society of London. A. Mathematical and Physical Sciences* 382 (1782): 43–59.
- 137 Qu, X., Xie, R., Zhou, Z. et al. (2023). Highly sensitive capacitive fiber pressure sensors enabled by electrode and dielectric layer regulation. *ACS Applied Materials & Interfaces* 15 (47): 54966–54976.
- 138 Yang, W., Ding, W., Liu, M. et al. (2021). A theoretical model of a flexible capacitive pressure sensor with microstructured electrodes for highly sensitive electronic skin. *Journal of Physics D: Applied Physics* 55 (9): 094001.
- 139 Zhang, Y., Lin, Z., Huang, X. et al. (2019). Highly sensitive capacitive pressure sensor with elastic metallized sponge. *Smart Materials and Structures* 28 (10): 105023.

- 140 Yang, J.C., Kim, J.O., Oh, J. et al. (2019). Microstructured porous pyramid-based ultrahigh sensitive pressure sensor insensitive to strain and temperature. *ACS Applied Materials & Interfaces* 11 (21): 19472–19480.
- 141 Larson, C., Peele, B., Li, S. et al. (2016). Highly stretchable electroluminescent skin for optical signaling and tactile sensing. *Science* 351 (6277): 1071–1074.
- 142 Wang, X., Li, T., Adams, J., and Yang, J. (2013). Transparent, stretchable, carbon-nanotube-inlaid conductors enabled by standard replication technology for capacitive pressure, strain and touch sensors. *Journal of Materials Chemistry A* 1 (11): 3580–3586.
- 143 Hu, W., Niu, X., Zhao, R. et al. (2013). Elastomeric transparent capacitive sensors based on an interpenetrating composite of silver nanowires and polyurethane. *Applied Physics Letters* 102 (8): 083303.
- 144 Liu, F., Han, F., Ling, L. et al. (2018). An omni-healable and highly sensitive capacitive pressure sensor with microarray structure. *Chemistry* 24 (63): 16823–16832.
- 145 Kim, H., Kim, G., Kim, T. et al. (2018). Transparent, flexible, conformal capacitive pressure sensors with nanoparticles. *Small* 14 (8): 1703432.
- 146 Baek, S., Jang, H., Kim, S.Y. et al. (2017). Flexible piezocapacitive sensors based on wrinkled microstructures: toward low-cost fabrication of pressure sensors over large areas. *RSC Advances* 7 (63): 39420–39426.
- 147 Ho, D.H., Sun, Q., Kim, S.Y. et al. (2016). Stretchable and multimodal all graphene electronic skin. *Advanced Materials* 28 (13): 2601–2608.
- 148 Boutry, C.M., Kaizawa, Y., Schroeder, B.C. et al. (2018). A stretchable and biodegradable strain and pressure sensor for orthopaedic application. *Nature Electronics* 1 (5): 314–321.
- 149 Gerratt, A.P., Sommer, N., Lacour, S.P., and Billard, A. (2014). Stretchable capacitive tactile skin on humanoid robot fingers—First experiments and results. In *2014 IEEE-RAS International Conference on Humanoid Robots*. IEEE. pp. 238–245.
- 150 Zhang, Y., Liu, S., Miao, Y. et al. (2020). Highly stretchable and sensitive pressure sensor array based on icicle-shaped liquid metal film electrodes. *ACS Applied Materials & Interfaces* 12 (25): 27961–27970.
- 151 Ha, K.H., Zhang, W., Jang, H. et al. (2021). Highly sensitive capacitive pressure sensors over a wide pressure range enabled by the hybrid responses of a highly porous nanocomposite. *Advanced Materials* 33: 2103320.
- 152 Qu, X., Li, J., Han, Z. et al. (2023). Highly sensitive fiber pressure sensors over a wide pressure range enabled by resistive-capacitive hybrid response. *ACS Nano* 17 (15): 14904–14915.
- 153 Ha, K.-H., Li, Z., Kim, S. et al. (2021). Stretchable hybrid response pressure sensors. *Matter* 7 (5): 1895–1908.
[https://www.cell.com/matter/fulltext/S2590-2385\(24\)00164-4](https://www.cell.com/matter/fulltext/S2590-2385(24)00164-4).
- 154 Lou, Z., Chen, S., Wang, L. et al. (2016). An ultra-sensitive and rapid response speed graphene pressure sensors for electronic skin and health monitoring. *Nano Energy* 23: 7–14.

- 155 Chen, W. and Yan, X. (2020). Progress in achieving high-performance piezoresistive and capacitive flexible pressure sensors: a review. *Journal of Materials Science and Technology* 43: 175–188.
- 156 Wang, H., Li, Z., Liu, Z. et al. (2022). Flexible capacitive pressure sensors for wearable electronics. *Journal of Materials Chemistry C* 10 (5): 1594–1605.
- 157 Huang, Y., Fan, X., Chen, S.C. et al. (2019). Emerging technologies of flexible pressure sensors: materials, modeling, devices, and manufacturing. *Advanced Functional Materials* 29 (12): 1808509.
- 158 Kumar, A. (2022). Recent progress in the fabrication and applications of flexible capacitive and resistive pressure sensors. *Sensors and Actuators A: Physical* 344: 113770.
- 159 Li, Z., Ha, K.H., Wang, Z. et al. (2022). Effects of AC frequency on the capacitance measurement of hybrid response pressure sensors. *Soft Matter* 18 (44): 8476–8485.